

THE HIGH VELOCITY GAS TOWARD MESSIER 5: TRACING FEEDBACK FLOWS IN THE INNER GALAXY

WILLIAM F. ZECH¹, NICOLAS LEHNER¹, J. CHRISTOPHER HOWK¹, W. VAN DYKE DIXON², & THOMAS M. BROWN³Accepted by the *ApJ*

ABSTRACT

We present *Far Ultraviolet Spectroscopic Explorer (FUSE)* and Space Telescope Imaging Spectrograph (STIS E140M) observations of the post-asymptotic giant branch star ZNG 1 in the globular cluster Messier 5 ($l = 3^{\circ}9$, $b = +47^{\circ}7$; $d = 7.5$ kpc, $z = +5.3$ kpc). High velocity absorption is seen in C IV, Si IV, O VI, and lower ionization species at LSR velocities of ~ -140 and ~ -110 km s⁻¹. We conclude that this gas is not circumstellar on the basis of photoionization models and path length arguments. Thus, the high velocity gas along the ZNG 1 sight line is the first evidence that highly-ionized HVCs can be found near the Galactic disk. We measure the metallicity of these HVCs to be $[O/H] = +0.22 \pm 0.10$, the highest of any known HVC. Given the clouds' metallicity and distance constraints, we conclude that these HVCs have a Galactic origin. This sight line probes gas toward the inner Galaxy, and we discuss the possibility that these HVCs may be related to a Galactic nuclear wind or Galactic fountain circulation in the inner regions of the Milky Way.

Subject headings: ISM: abundance — ISM : clouds — ISM: structure — stars: individual (NGC 5904 ZNG 1) — ultraviolet : ISM

1. INTRODUCTION

High-velocity clouds (HVCs) are identified because they are clearly inconsistent with participating in Galactic rotation. In practice, the cut-off for selecting HVCs is that they have LSR velocities $|v_{\text{LSR}}| \geq 90$ km s⁻¹. While their origins are not fully understood, there is growing evidence that the HVCs are important components of the on-going exchange of matter between the Milky Way and the surrounding intergalactic medium (IGM) and, therefore, important to our understanding of the formation and evolution of galaxies (see, e.g., the recent reviews by Wakker et al. 1997, 1999; Wakker 2004; Benjamin 2004; Richter 2006). In this context, many models have been constructed for the HVCs. Oort (1970) first suggested the HVCs were gaseous relics left over from the formation of the Milky Way, and more recent models have elaborated on this model of HVCs as the building blocks of galaxies and the Local Group (Blitz et al. 1999). The discovery of disrupted stellar satellites in the halo of the Milky Way has led to suggestions that HVCs may be the gaseous remnants of such satellites accreted by the Galaxy (Ibata et al. 1994; Putman et al. 2004), and the Magellanic Stream has long been known as gas removed from the Magellanic Clouds (Putman et al. 2003). Various models (e.g., Bregman 1978, Houck & Bregman 1990) have also discussed the HVCs in the context of the galactic fountain, in which gas is ejected from the Galactic disk by the combined effects of multiple, correlated supernova explosions (Shapiro & Field 1976; Norman & Ikeuchi 1989). These models have distinct predictions for the distances and metallicities of the HVCs. These are the two principal diagnostics for the origins of the HVCs.

Over the last decade, observations with the *Hubble Space Telescope (HST)*, the *Far Ultraviolet Spectroscopic*

Explorer (FUSE), and some ground-based instruments have provided measurements of the metallicities and distance brackets for some of the major neutral HVC complexes. The general picture that has emerged for these prominent neutral complexes (e.g., complexes A and C) is one in which they have an extragalactic origin given their low metallicities (e.g., complex C has a metallicity $\sim 15\%$ solar; Collins et al. 2007, see van Woerden & Wakker 2004 for a summary) and distances from the sun bracketed to be within $5 \lesssim d \lesssim 12$ kpc (e.g., Thom et al. 2006, 2007; Wakker et al. 2007a,b; van Woerden et al. 1999). The Magellanic Stream is another example, thought to be at $d \sim 50 - 75$ kpc with a metallicity $\sim 25\%$ that of the sun (Gibson et al. 2000, Sembach et al. 2001).

Traditionally, HVCs were observed via optical or radio observations (e.g., Münch 1952; Münch & Zirin 1961, Wakker 1991). These clouds were therefore known as neutral entities. However, UV observations from *HST* and *FUSE* as well as ground-based H α observations (Tufte et al. 2002, Putman et al. 2003), have revealed a significant ionized component of the neutral complexes. Furthermore, such data have also allowed the discovery of a new class of HVCs without H I emission, the highly-ionized HVCs (Sembach et al. 1999, 2003; Lehner et al. 2001, Lehner 2002; Collins et al. 2004, 2005; Ganguly et al. 2005; Fox et al. 2006). These HVCs show absorption from the “high ions” O VI, N V, C IV, and Si IV; these ions require large energies for their production, and O VI, in particular, cannot be produced via photoionization within the Galaxy (e.g., Sembach et al. 2003), suggesting the presence of hot gas to provide for the ionization. Some of the highly-ionized high velocity absorption seen towards AGNs is associated with the outer layers of known H I HVC complexes based on their coincidental velocities and proximity on the sky (e.g., gas associated with the outer edges of complexes A, C, and the Magellanic Stream; Sembach et al. 2003, Fox et al. 2004, 2005). However, others have no H I 21-cm emission, and therefore are not part of large neutral com-

¹ Department of Physics and Astronomy, University of Notre Dame, Notre Dame, IN, 46556

² Department of Physics and Astronomy, The Johns Hopkins University, Baltimore, MD, 21218

³ Space Telescope Science Institute, Baltimore, MD, 21218

plexes. They do, however, show H I and C III *absorption* counterparts, implying they have a multiphase structure (Fox et al. 2006 and references therein).

The origin of these highly-ionized HVCs are mostly unknown because neither their distances nor their metallicities are well known. Up to this work, there has been no report of highly-ionized HVCs observed in absorption against distant Milky Way stars (Zsargó et al. 2003), the only way to directly constrain the distances to HVCs. This, together with kinematic arguments (Nicastró et al. 2003), led Nicastró (2005) to conclude that these HVCs must be extragalactic since the highly-ionized HVCs are detected only toward AGNs and QSOs. However, early-type stars often have complicated spectra near the high ions, and absorption from a highly-ionized HVC could easily be lost in the complicated structure of the continuum, especially if the absorption is weak. The metallicities of highly-ionized HVCs are also difficult to determine. Since they are defined by their ionization state, the ionization corrections required to determine the metallicities are often large and extremely model dependent. For the majority of these clouds, the distance and metallicity estimates rely on photoionization models based on an assumed ionizing spectrum (e.g., Sembach et al. 1999, Collins et al. 2004, 2005, Ganguly et al. 2005, and others). These studies have suggested the clouds are located in the distant reaches of the Milky Way (e.g., Collins et al. 2005, Fox et al. 2006) and have significantly sub-solar metallicities, typically $\sim 20\%$ solar with a range of 4% to 40% solar. Prior to the present work, there have only been three metallicity limits for highly-ionized HVCs using the columns of O I and H I (Fox et al. 2005, Ganguly et al. 2005), a comparison that does not require ionization corrections to derive the metallicity. These upper limits are mostly crude, consistent with both solar and sub-solar abundances.

In view of the uncertainties in their properties, the highly-ionized HVCs are consistent with both an extragalactic or Galactic origin. In particular, they may trace a hot Galactic fountain (Fox et al. 2006) or, in cases where the sight line passes near the Galactic center, a nuclear wind (Keeney et al. 2006). Galactic nuclear winds are observed in external galaxies across the electromagnetic spectrum (Martin 1999; Strickland 2002; Heckman 2002; Veilleux 2002), and there is evidence that the Milky Way also has a Galactic nuclear wind (Bland-Hawthorn & Cohen 2003). Analyses of X-ray observations toward the Galactic center have provided further evidence for an outflow from the central regions of the Galaxy (Almy et al. 2000; Sofue 2000; Yao & Wang 2007). Such a Galactic outflow/wind should be detectable via UV high-ion absorption not only in the spectra of QSOs but also in distant stars at high galactic latitudes. Keeney et al. (2006) discussed the possibility that a wind from the Galactic center may give rise to highly-ionized HVC absorption seen in the spectra of two AGNs. The subsolar metallicities they attribute to these absorbers are at odds with a Galactic wind origin. However, if, as they suggest, their photoionization models provide inappropriate metallicity estimates, there may yet be reason to believe these HVCs probe the expulsion (and perhaps subsequent return) of matter from the inner regions of the Milky Way.

In this work, we present new observations of a highly-ionized HVC that is located toward the inner Galaxy

at a distance from the sun $d < 7.5$ kpc and height above the Galactic plane $z < 5.3$ kpc. This HVC is detected in the *FUSE* and Space Telescope Imaging Spectrograph (STIS) spectra of the post-asymptotic giant branch (PAGB) star ZNG 1 located in the globular cluster Messier 5 (NGC 5904, $d = 7.5$ kpc). This is the first highly-ionized HVC for which the upper limit on the distance is known. This HVC was first reported by Dixon et al. (2004), but its origin (circumstellar or truly interstellar gas) was not fully explored in their work. Here we rule out the circumstellar origin and show the gas has a supersolar metallicity, which is consistent with an origin in the inner Galaxy. This is the first highly-ionized HVC unambiguously detected in the spectrum of a Galactic star, and this HVC has the highest measured metallicity of any yet studied.

This paper is structured as follows. We summarize the *FUSE* and STIS observations and our reduction of the data in § 2, and in § 3 we discuss the properties of the star and sight line. We present our measurements of the observed high velocity absorption in § 4. In § 5 we discuss the physical properties of the high velocity gas including the electron density, ionization fraction, and metallicity. We analyze the kinematics and ionization mechanisms involved with the gas along the ZNG 1 sight line in § 6. We use photoionization modeling and path length arguments to rule out the circumstellar hypothesis for the origin of the high velocity gas toward ZNG 1 in § 7. In § 8 we discuss our results in the context of a Galactic circulation/feedback and suggest further research to test this hypothesis, and we discuss the implications for other highly-ionized HVCs. We summarize our principal conclusions in § 9.

2. OBSERVATIONS AND REDUCTIONS

The observations for this work were taken from STIS on board *HST* and *FUSE*. In the following subsections, we discuss the data reduction and handling procedures for the STIS and *FUSE* spectral data sets.

2.1. STIS

The STIS observations were made between July 8 and July 19, 2003 under the Guest Observer program 9410. Five visits were made with identifications O6N40401–402, and O6N40301–303 for a total exposure time of 12.8 ks. The STIS observations of ZNG 1 were taken in the ACCUM mode with the $0'.2 \times 0'.2$ aperture using the E140M echelle grating to disperse the light onto the far-ultraviolet Multi-Anode Microchannel-Array (MAMA) detector. The usable wavelength coverage is from ~ 1150 Å to 1710 Å. The resolution of this mode is $R \equiv \lambda/\Delta\lambda \sim 45,800$ corresponding to a velocity FWHM of ~ 6.5 km s $^{-1}$ with a detector pixel size of 3.22 km s $^{-1}$. The STIS data were retrieved from the Multimission Archive at Space Telescope (MAST), and reduced with the CALSTIS (Version 2.14c; Brown et al. 2002) pipeline in order to provide orbital Doppler shift adjustments, detector nonlinearity corrections, dark image subtraction, flat field division, background subtraction, wavelength zero-point calibration, and to convert the wavelengths into the heliocentric reference frame. The individual exposures were weighted by their inverse variance and combined into a single spectrum. For a description of the design and construction of STIS see Woodgate et al.

(1998), and a summary of the STIS on-orbit performance is given by Kimble et al. (1998).

We applied a shift of $\Delta v_{\text{LSR}} = v_{\text{LSR}} - v_{\text{helio}} = +13.25$ km s⁻¹ to the data to transform the heliocentric velocities provided by STIS to the local standard of rest (LSR) frame. This assumes a solar motion of +20 km s⁻¹ in the direction $(\alpha, \delta)_{1900} = (18^{\text{h}}, +30^{\circ})$ [$(l, b) \approx (56^{\circ}, +23^{\circ})$] (Kerr & Lynden-Bell 1986). For comparison, the Mihas & Binney (1981) definition of the LSR gives a velocity shift of $\Delta v_{\text{LSR}} = +11.76$ km s⁻¹. The velocity uncertainty of the STIS observations is ~ 1 km s⁻¹ with occasional errors as large as ~ 3 km s⁻¹ (see the Appendix of Tripp et al. 2005).

2.2. FUSE

The *FUSE* observations were made under programs A108 and D157 on July 15, 2000 and between April 11 – 13, 2003 for a total of four visits. The *FUSE* data sets are A1080303 and D1570301–303, and the total exposure time is 30.4 ks. The four *FUSE* observations of ZNG 1 were taken using the LWRS 30'' \times 30'' apertures in the photon event (TTAG) mode. The wavelength range of the data is 905 Å to 1187 Å with a resolution of ~ 20 –25 km s⁻¹ and a binned output pixel size of 3.74 km s⁻¹. The data were reduced using the CalFUSE (Version 3.1.3) pipeline. The CalFUSE processing is described in Dixon et al. (2007), and the spectroscopic capabilities and early on-orbit performance of *FUSE* are described in Moos et al. (2000) and Sahnou et al. (2000), respectively.

Data were obtained from the SiC1, SiC2, LiF1, and LiF2 channels. For each *FUSE* segment, the intermediate data files produced by CalFUSE were shifted to a common wavelength scale and combined into a single file. Time segments exhibiting a low count rate, e.g., when the target fell near the edge of the spectrograph apertures, were excluded from further consideration. The detector and scattered-light background were scaled and subtracted by CalFUSE. The *FUSE* relative wavelength is accurate to roughly ± 5 km s⁻¹ but can vary by 10 – 15 km s⁻¹ over small wavelength intervals. The absolute zero point of the wavelength scale for the individual absorption lines is uncertain and was determined using the well-calibrated STIS data. Where possible, transitions from the same species were compared (e.g., Fe II $\lambda\lambda 1055, 1063$ were aligned with Fe II $\lambda\lambda 1608, 1611$). Where this was not possible, we compared different ions with similar ionization potentials and similar absorption depths (e.g., Ar I $\lambda\lambda 1055, 1066$, with N I $\lambda\lambda 1199, 1200$). For the ion O VI we aligned and coadded the data from the LiF1A, LiF2B, SiC1A, and SiC2B channels. No ion was available to directly fix the velocity scale of O VI. However, the shifts for transitions throughout the LiF1A segment were all consistent, and we adopted their average to align O VI. Based on a comparison of the velocity centroids of the H₂ lines $\lambda\lambda 1009, 1013, 1026, 1031$ near O VI in *FUSE*, we conclude that no additional velocity shift for O VI was needed.

3. THE M5 ZNG 1 SIGHT LINE

ZNG 1 is a post-asymptotic giant branch star in the globular cluster M5 (NGC 5904); the properties of the star and cluster are summarized in Table 1. ZNG 1 has a remarkably fast projected rotational velocity for a PAGB star ($v \sin i = 170$ km s⁻¹). One possible explanation

TABLE 1
PARAMETERS OF M5-ZNG 1

Parameter	Value	Reference ^a
Cluster Parameters		
Distance	7.5 kpc	3
[Fe/H]	-1.27	3
v_{LSR}	+65.7 km s ⁻¹	3
Stellar Parameters		
Spectral type	sdO	1
V	14.54	2
$B - V$	-0.32	2
$E(B - V)$	0.03	3
T_{eff}	44300 \pm 300 K	4
$\log g$	4.3 \pm 0.1	4
$v \sin i$	170 \pm 20 km s ⁻¹	4
v_{LSR}	+51 \pm 3 km s ⁻¹	5
$\log L/L_{\odot}$	3.52 \pm 0.04	4
M/M_{\odot}	0.69 \pm 0.17	4
C abundance ^b	2.58 \pm 0.20%	4
N abundance	0.51 \pm 0.05%	4
O abundance	0.37 \pm 0.32%	4

^a References: (1) Napiwotzki & Heber 1997; (2) Piotto 2002; (3) Harris 1996 (on-line version dated February 2003); (4) Dixon et al. 2004; (5) This work.

^b Abundances are quoted as mass fractions.

may be that this star has been spun up by a merger with a binary companion. This star has very little hydrogen in its atmosphere, with a helium abundance of 99% by number (W. V. Dixon, unpublished). Its photospheric carbon and nitrogen abundances are 10 times solar by mass, suggesting products of helium burning were mixed to the surface while the star was on the AGB (Dixon et al. 2004). The sight line to this star shows high velocity absorption as first noted by Dixon et al. (2004). Over the velocity range $-162 < v_{\text{LSR}} < -90$ km s⁻¹, absorption from the ions H I, C II, C IV, N II, O I, O VI, Al II, Si II, Si III, Si IV, S III, and Fe II is seen in our STIS and *FUSE* observations (see Figures 1, 2, and 3). The presence of strong Si IV, C IV, and O VI absorption at high velocities ($|v| \gtrsim 100$ km s⁻¹) place these clouds in the category of highly-ionized HVCs recently discussed by Fox et al. (2005), Collins et al. (2004; 2005), and Ganguly et al. (2005). High velocity absorption is detected in multiple components with centroid LSR velocities at roughly -110 km s⁻¹ and -140 km s⁻¹ (-190 km s⁻¹ and -160 km s⁻¹ relative to the photosphere of ZNG 1). Our aim is to determine the origin of this observed multiphase high-velocity absorption.

The sight line to M5 ZNG 1 probes a 7.5 kpc path toward the inner Galaxy. It passes through Radio Loop I (centered at roughly $l = 329^{\circ}0$, $b = 17^{\circ}5$ with a diameter of $\sim 116^{\circ}$, Berkhuijsen et al. 1971). The energy source for the Loop I superbubble is commonly thought to be stellar winds and/or supernovae in the Sco-Cen OB association located at a distance of $d \sim 170$ pc from the sun (Park et al. 2007; Wolleben 2007 and references therein).⁴ It is a priori possible that the high velocity ab-

⁴ Loop I is typically associated with the Sco-Cen OB association; however, Bland-Hawthorn & Cohen (2003) and Yao & Wang (2007) argue that the North Polar Spur (NPS), which is usually thought to be a part of Loop I, is actually a limb brightened LSR region associated

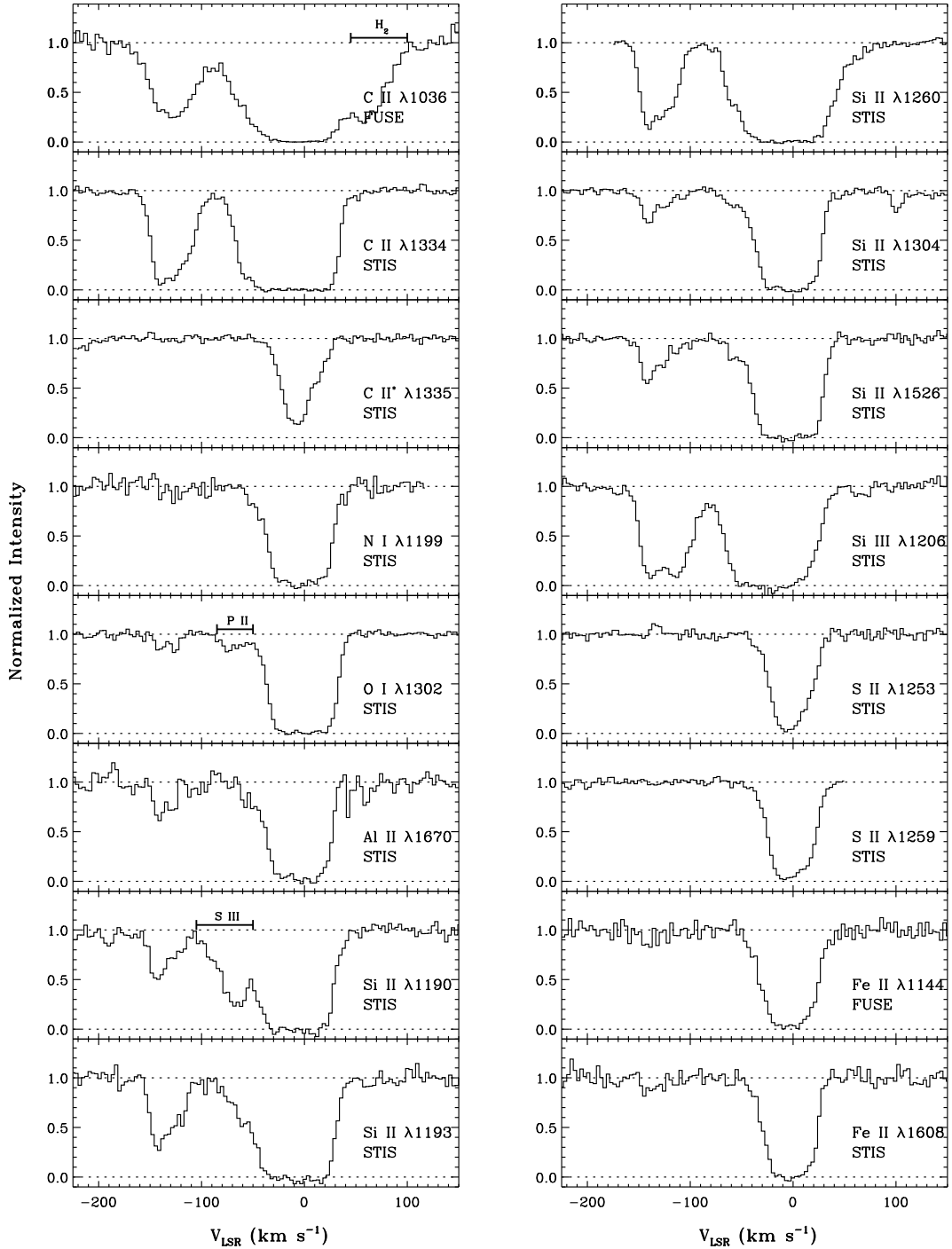


FIG. 1.— Normalized intensity profiles of the tracers of the low ions. The HVC region lies in the velocity range -160 km s^{-1} to -90 km s^{-1} with centroid velocities for C IV and Si IV at -142 km s^{-1} and -111 km s^{-1} . Gas participating in the global rotation of the Galaxy is observed at $|v_{\text{LSR}}| \lesssim 30 \text{ km s}^{-1}$. The instrument from which the data were taken is identified in the lower right of each profile. *FUSE* has a resolution of $\sim 20 \text{ km s}^{-1}$ and STIS E140M has a resolution of 6.5 km s^{-1} .

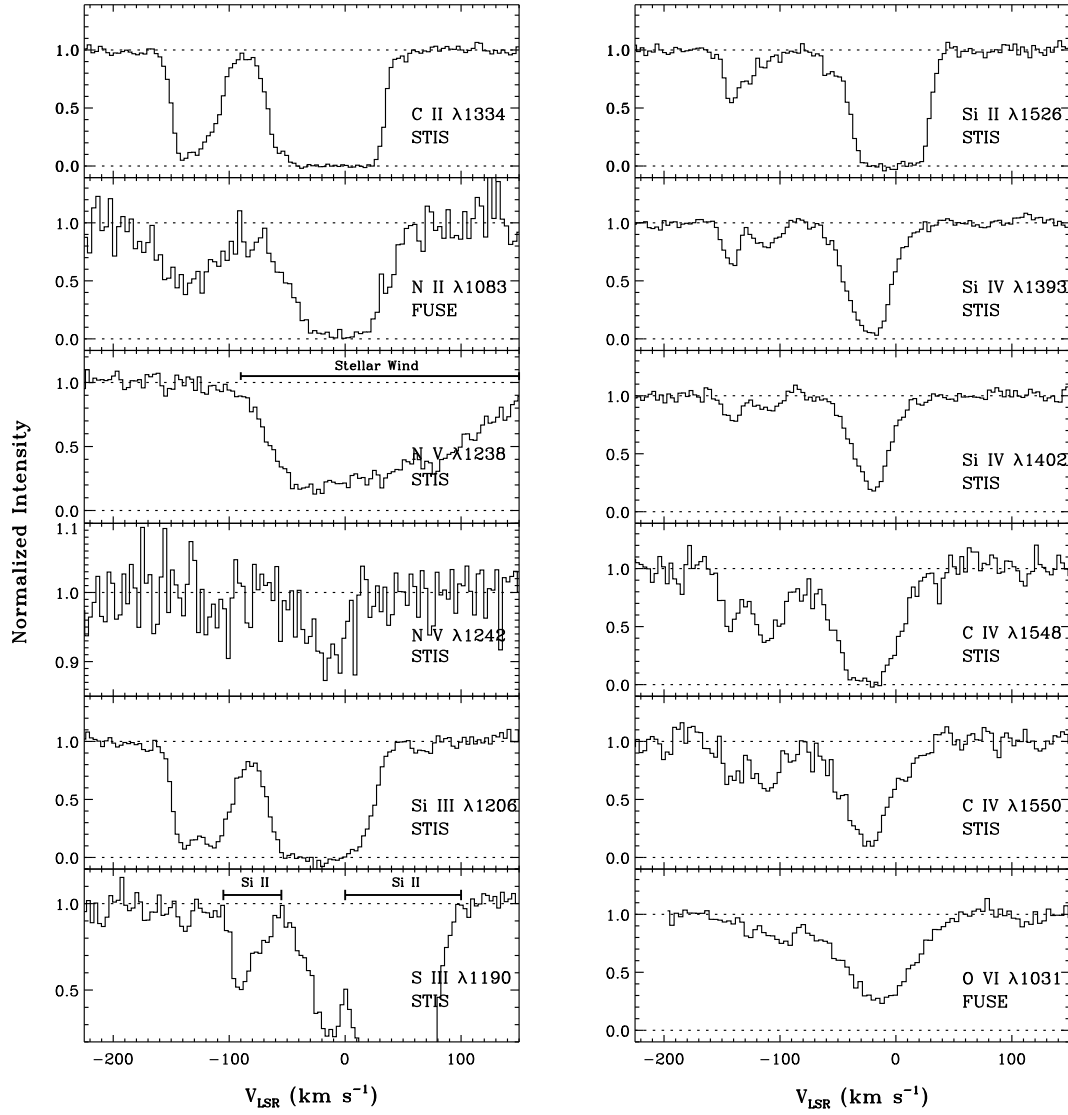


FIG. 2.— Same as Figure 1 but for the ions that are doubly or more ionized. The C II, N II, and Si II profiles are for comparison (although note that N II solely probes ionized gas).

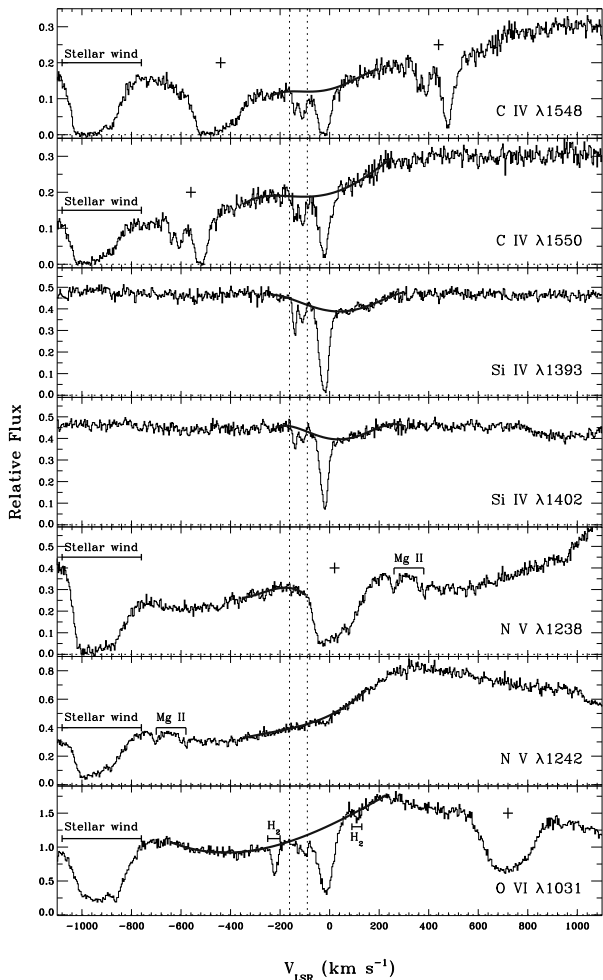


FIG. 3.— Adopted continuum fits of the high ions are shown as the solid black curves. The fits to the continua for the C IV and Si IV lines were adopted from the component fitting software. The two vertical lines show the HVC region of interest. The P-Cygni profile with a terminal velocity of ~ 900 km s $^{-1}$ is clearly seen in the C IV, N V, and O VI lines. The plus signs represent the profiles and/or stellar wind features of the other line of the doublet. We do not use N V $\lambda 1238$ in our analysis due to the difficulty in determining the continuum. We show it here to demonstrate this difficulty and show the stellar wind profile.

sorption toward ZNG 1 may be associated with material in Loop I.

Savage & Lehner (2006) analyzed the O VI in the sight lines to 39 white dwarfs, of which 3 lie in the direction of Loop I at low latitudes with distances close to 200 pc. No O VI is observed in any of these sight lines at high velocities. Sembach et al. (1997) observed the sight line toward HD 119608 ($l = 320^{\circ}.4$, $b = 43^{\circ}.1$) that passes through Loop I. In addition, they compiled archival *IUE* observations of ~ 20 sight lines passing through Loop I. Again, no high-ion absorption was detected at high velocities. The sight line to 3C 273 passes through Loop I which shows very strong C IV and O VI absorption with velocities between roughly -100 and $+100$ km s $^{-1}$ (Sem-

bach et al. 2001, 1997); a high velocity wing feature is also seen, reaching as far as $+240$ km s $^{-1}$ (Sembach et al. 2001). Given that the sight lines which probe O VI in or near Loop I show no absorption at high negative velocities, it is unlikely that the high velocity gas toward ZNG 1 represents Loop I material. We note also that the [O/H] of the ISM within 800 pc is observed to be nearly solar (Cartledge et al. 2004). If the HVCs toward ZNG 1 were to represent Loop I material, one would expect the metallicity to more closely match that of the local neighborhood. The super-solar metallicity of the HVCs toward ZNG 1 (see § 5.2), combined with the absence of HVCs with $v_{\text{LSR}} \leq -100$ km s $^{-1}$, strongly suggest that they reside farther than the ~ 200 pc distance of Loop I.

The Leiden-Argentine-Bonn (LAB) Survey (Kalberla et al. 2005) provides us with a neutral hydrogen column density of $N(\text{H I}) = 3.67 \times 10^{20}$ cm $^{-2}$ for H I emission centered around $v_{\text{LSR}} \approx 0$ km s $^{-1}$ in the direction of M5. A perusal of the survey reveals no H I emission at velocities $|v_{\text{LSR}}| \gtrsim 30$ km s $^{-1}$ within 10° of ZNG 1 with a sensitivity of $N(\text{H I}) \approx 3 \times 10^{18}$ cm $^{-2}$ for an HVC FWHM ~ 20 km s $^{-1}$.⁵ The high velocity gas seen toward ZNG 1 is not clearly associated with any known HVC complex (Wakker 2001). The closest HVC complex is complex L ($\Delta\theta \sim 25^{\circ} - 30^{\circ}$) which has a mean LSR velocity ~ -115 km s $^{-1}$. Richter et al. (2005) find HVC absorption toward PKS 1448-232 ($l = 335^{\circ}.4$, $b = +31^{\circ}.7$, $\Delta\theta \sim 27^{\circ}$ from ZNG 1) with LSR velocities near -100 , -130 , and -150 km s $^{-1}$ that are similar to those observed in the HVCs toward ZNG 1. Richter et al. attribute this absorption to complex L. The compact HVC CHVC 018.3-47.1-147 (de Heij et al. 2002) lies $\sim 10^{\circ}$ from ZNG 1 with an LSR velocity of -147 km s $^{-1}$ (this is cloud 57 in Wakker & van Woerden 1991).

Zsargó et al. (2003) analyzed *FUSE* spectra for 22 Galactic halo stars. They saw no clear evidence of high velocity O VI in any of the sight lines. Their sample included ZNG 1; however, they used earlier *FUSE* data for this star with a S/N of about half of that of our data. ZNG 1 is the only known Galactic sight line to show highly-ionized interstellar HVCs.

Sembach et al. (2003), in their survey of high velocity O VI, analyzed highly-ionized high velocity gas along sight lines to 100 extragalactic objects and 2 halo stars. Of the sight lines in their study, only Mrk 1383 ($l = 349^{\circ}.2$, $b = +55^{\circ}.1$, $\Delta\theta = 11^{\circ}.8$ from ZNG 1) lies within 30° of ZNG 1. Mrk 1383 shows no blueshifted high velocity absorption (Keeney et al. 2006; Sembach et al. 2003). Fox et al. (2006) analyzed the spectra of 66 extragalactic sight lines searching for highly-ionized HVCs. The sight line toward PG 1553+113 ($l = 21^{\circ}.9$, $b = +44.0$, $\Delta\theta = 13^{\circ}.1$) shows O VI absorption at blueshifted velocities between -170 and -100 km s $^{-1}$ (e.g., see Figure 6 of Fox et al. 2006, § 8). Fox et al. (2006) reported a 3σ upper limit for the O VI absorption at negative LSR velocities (-200 to -100 km s $^{-1}$). The main difference between our analysis and theirs is the velocity range used to estimate the equivalent width and column density: Considering the velocity range $v_{\text{LSR}} = -200$ to -100 km s $^{-1}$, the 3σ upper limit on the equivalent width

⁵ The brightness-temperature sensitivity of the LAB survey is $0.07\text{--}0.09$ K with a sensitivity of $N(\text{H I}) \approx 2 \times 10^{17}$ cm $^{-2}$ per 1.3 km s $^{-1}$ resolution element.

is 40 mÅ. Between -170 and -100 km s $^{-1}$, we measure $W_\lambda = 39 \pm 11$ mÅ and $\log N(\text{O VI}) = 13.57_{-0.13}^{+0.11}$, corresponding to a 3.5σ detection.

Given its evolutionary status, this star may be expected to have circumstellar material, perhaps even a (proto) planetary nebula (PN). Dixon et al. (2004) have summarized the prior observations of ZNG 1 and the search for a PN. Bohlin et al. (1983) suggested that an apparent N IV $\lambda 1478$ emission feature in the *IUE* spectrum of ZNG 1 was a signature of a PN. However, using an analysis of the complete archival *IUE* data, de Boer (1985) argued the apparent N IV feature was not real; he did note the P-Cygni profile of the N V $\lambda\lambda 1238, 1242$ doublet, a sign of an outflowing wind from the star. This wind shows a terminal velocity of ~ 900 km s $^{-1}$ (e.g., see Figure 3 and Dixon et al. 2004). Napiwotzki & Heber (1997) set out to test the PN hypothesis by using *HST* to obtain a WFPC2 H α image. The H α image revealed no evidence for extended emission around the star from a PN. Any circumstellar H α is constrained to lie within $0.2''$ (7×10^{-3} pc) from the star. We will present strong evidence against the possibility that the HVCs in this direction are associated with circumstellar material in § 7.

At Galactic coordinates $l = 3^\circ.9$, $b = +47^\circ.7$, a distance of $d = 7.5$ kpc (Harris 1996), and a vertical distance above the Galactic plane of $z = +5.3$ kpc, ZNG 1 lies about 3.5 kpc from the rotation axis of the Galaxy. At this location, a Galactic bipolar wind, for which evidence has been accumulating recently, may play a role in this HVC material. Almy et al. (2000) analyzed *ROSAT* X-ray observations toward Loop I and the Galactic center and were able to show that a large fraction ($45\% \pm 9\%$) of the X-ray emission originates beyond $d \sim 2$ kpc. They suggested that the most probable source for this emission was the Galactic X-ray “bulge.” Yao & Wang (2007) used a differential analysis of archival *Chandra* grating observations of the sight lines toward Mrk 421 ($l = 179^\circ.8$, $b = 65^\circ.0$) and 3C 273 ($l = 290^\circ.0$, $b = 64^\circ.4$) to obtain the net emission and absorption of the hot gas toward the Galactic center soft X-ray emission (seen toward 3C 273). They showed that the X-ray emitting gas toward 3C 273 originated beyond 200 pc and suggested the most likely source was a Galactic center outflow. If this X-ray emission indeed originates from the Galactic center, then the Galactic latitude of 3C 273 ($b = 65^\circ.0$) suggests that an outflow can reach beyond the Galactic latitude of ZNG 1 ($b = 47^\circ.7$). Based on the 408 MHz radio continuum and the *ROSAT* all-sky soft X-ray data, Sofue (2000) calculated the expected size of an outflow. His predictions for the outer boundary of an outflow encompass ZNG 1. Furthermore, ZNG 1 is located inside the outflow cones in the empirically-motivated models of Bland-Hawthorn & Cohen (2003). Keeney et al. (2006) have previously discussed a Galactic wind in the context of the highly-ionized HVCs toward Mrk 1383 and PKS 2005–489, attributing the HVCs to a Galactic center outflow. The sight line toward ZNG 1 may intercept material associated with feedback-driven flows in the central regions of the Galaxy, either from a nuclear wind or from Galactic fountain-type flows from the inner Galaxy. We discuss this possibility in § 8.

4. INTERSTELLAR ABSORPTION LINE MEASUREMENTS

We have measured column densities, equivalent widths, b -values, and signal-to-noise ratios for the ion profiles where significant absorption is seen in the HVC region. Where the absorption is absent and not contaminated, 3σ upper limits for the column densities and equivalent widths were calculated. We employed two principal methods in obtaining these values, the apparent optical depth (AOD) method as described by Savage & Sembach (1991) and a component fitting method as described by Fitzpatrick & Spitzer (1997), discussed in § 4.1 and § 4.2, respectively. We separately discuss our analysis of the H I Lyman series absorption in § 4.3.

4.1. AOD Measurements of the Metal Lines

Figures 1 and 2 show the normalized intensity profiles for the low and high ions, respectively. We normalized each absorption feature by fitting a low-order (≤ 5) Legendre polynomial to the adjacent continuum. The continuum of ZNG 1 for the most part was easily modeled, with the exception of the regions about Si IV and C IV. The C IV 1548, 1550 Å doublet lies in the presence of a stellar wind making the continuum placement more difficult. The Si IV 1393, 1402 Å lines each lie in a stellar feature with the added complication that the Si IV $\lambda 1402$ line lies near the edge of a spectral order. The data from the spectral orders for the 1402 Å line were coadded, however, there was a feature near -85 km s $^{-1}$ which appeared in one order but not the other. For these high ions, we adopt continua determined through a component fitting analysis, the details of which are described in § 4.2. Figure 3 shows the adopted continua for the ions C IV $\lambda\lambda 1548, 1550$, Si IV $\lambda\lambda 1393, 1402$, N V $\lambda\lambda 1238, 1242$ and O VI $\lambda 1031$. While continuum placement near the O VI $\lambda 1031$ line can sometimes be problematic in stars, here the continuum is well determined. We cannot use the O VI $\lambda 1037$ line because it is always contaminated by C II, C II*, and H $_2$.

The strong line of O VI at 1031 Å can be contaminated by H $_2$ or HD lines from the Milky Way, and by Cl I at 1031 Å. The Cl I is at -122 km s $^{-1}$ with respect to O VI which is in the velocity region of our HVCs. We searched for absorption from Cl I $\lambda\lambda 1004, 1003$, which have similar strengths to the 1031 transition, and found none. Of the three molecular lines that can contaminate O VI, HD 6–0 R(0) $\lambda 1031$, (6–0) P(3) $\lambda 1031$, and R(4) $\lambda 1032$, are at -4 , -214 and $+125$ km s $^{-1}$ relative to O VI, respectively, and are not in the velocity region of our HVCs.

Table 2 gives our measured properties of the high-velocity interstellar absorption lines toward ZNG 1, including the equivalent widths, apparent column densities, signal-to-noise, and b -values. Table 3 gives the column densities and b -values for the two components seen in the high ions. We measured equivalent widths of interstellar features following Sembach & Savage (1992) including their treatment of the uncertainties. We assumed statistical uncertainties for the *FUSE* data were dominated by the effects of fixed pattern noise, while the uncertainties for the STIS data were treated as statistical Poisson uncertainty. In addition, we include an uncertainty in the placement of the continuum added in quadrature to the statistical uncertainty following Sembach & Savage (1992).

The column densities quoted here are derived from

TABLE 2
INTERSTELLAR ABSORPTION LINES TOWARDS M5-ZNG 1

Species	λ [Å]	$\log \lambda f$	W_λ [mÅ]	$\log N_a$ [cm ⁻²]	Δv^a [km s ⁻¹]	b_a [km s ⁻¹]	S/N ^b	Instrument
C II	1334.532	2.234	177 ± 2	> 14.27	-162, -90	17.9 ± 0.2	31	STIS
C II	1036.337	2.088	131 ± 5	> 14.26	-162, -90	22.3 ± 0.7	16	FUSE/LiF 1A
C II*	1335.708	2.186	< 5	< 12.44	-162, -90	...	42	STIS
C IV	1548.195	2.468	144 ± 6	13.70 ± 0.04	-162, -90	24.4 ± 1.0	12	STIS
C IV	1550.770	2.167	92 ± 6	13.74 ± 0.03	-162, -90	24.7 ± 1.3	14	STIS
N I ^c	1199.550	2.199	< 12	< 12.82	-162, -90	...	17	STIS
N II	1083.994	2.079	102 ± 12	> 14.07	-162, -90	23.9 ± 2.5	6	FUSE/SiC 1A
N II**	1085.550	1.286	< 29	< 14.19	-162, -90	...	6	FUSE/SiC 1A
N II**	1085.710	2.000	< 25	< 13.41	-162, -90	...	7	FUSE/SiC 1A
N V	1242.804	1.985	< 8	< 12.84	-162, -90	...	27	STIS
O I	1302.168	1.796	16 ± 3	13.38 ± 0.08	-162, -85	20.8 ± 5.0	38	STIS
O VI	1031.926	2.136	33 ± 3	13.46 ± 0.04	-162, -90	25.6 ± 2.3	23	FUSE ^d
Al II	1670.787	3.463	50 ± 8	12.11 ± 0.07	-162, -90	20.4 ± 3.6	11	STIS
Si II	1190.416	2.541	54 ± 3	> 13.27	-162, -110	14.8 ± 0.7	18	STIS
Si II	1193.290	2.842	86 ± 4	> 13.23	-162, -100	15.7 ± 0.7	18	STIS
Si II	1260.422	3.171	133 ± 3	> 13.15	-162, -90	17.3 ± 0.4	37	STIS
Si II	1304.370	2.052	36 ± 2	13.49 ± 0.03	-162, -90	18.1 ± 1.4	40	STIS
Si II	1526.707	2.307	63 ± 3	13.43 ± 0.03	-162, -90	19.2 ± 1.3	29	STIS
Si III	1206.500	3.293	197 ± 3	> 13.30	-162, -85	22.0 ± 0.3	21	STIS
Si IV	1393.755	2.854	50 ± 3	12.81 ± 0.02	-162, -90	23.3 ± 1.0	33	STIS
Si IV	1402.770	2.552	30 ± 3	12.86 ± 0.04	-162, -90	21.8 ± 1.8	28	STIS
S II	1253.811	1.135	< 8	< 13.67	-162, -90	...	28	STIS
S II	1259.519	1.311	< 6	< 13.39	-162, -90	...	36	STIS
S III	1190.208	1.421	12 ± 3 ^e	13.67 ± 0.10 ^e	-162, -105	18.8 ± 4.2	18	STIS
Fe II	1144.938	1.978	14 ± 5	13.19 ± 0.13	-162, -90	24.7 ± 8.2	15	FUSE/LiF 1B
Fe II	1144.938	1.978	13 ± 5	13.15 ± 0.14	-162, -90	...	16	FUSE/LiF 2A
Fe II	1608.451	1.968	14 ± 6	13.07 ± 0.02	-162, -90	...	16	STIS

NOTE. — Wavelengths and f -values are from Morton (2003). Upper limits are 3σ estimates; a b -value of 20 km s⁻¹ was assumed when no data were available.

^a Δv denotes the integration range. Where the range differs from -162 to -90 km s⁻¹ we have adjusted for nearby contaminating absorption.

^b The quoted value is the signal to noise ratio per detector pixel. For STIS, the detector has a pixel size of 3.22 km s⁻¹ per pixel and *FUSE*, the detector has an output pixel size of 3.74 km s⁻¹ per pixel.

^c The other members of these multiplets were blended with a stellar or interstellar features and are not included in this table.

^d The *FUSE* data used for this measurement are the coaddition of data from the LiF 1A, LiF 1B, SiC 1A, and SiC 2B segments.

^e This line may be slightly contaminated by Si II λ 1190.

TABLE 3
HIGH ION COMPONENT INTEGRATIONS^a

Species	λ [Å]	Component 1 ^b		Component 2 ^c	
		$\log N_a$ [cm ⁻²]	b_a^d [km s ⁻¹]	$\log N_a$ [cm ⁻²]	b_a^d [km s ⁻¹]
C IV	1548.195	13.25 ± 0.05	11.0 ± 1.1	13.50 ± 0.02	12.2 ± 0.5
C IV	1550.770	13.35 ± 0.05	12.2 ± 1.3	13.53 ± 0.04	12.2 ± 0.8
N V	1242.804	< 12.73	... ^e	< 12.75	...
O VI	1031.926	12.92 ± 0.08	14.4 ± 2.4	13.34 ± 0.03	15.6 ± 0.8
Si IV	1393.755	12.58 ± 0.03	7.8 ± 1.1	12.44 ± 0.04	11.6 ± 1.0
Si IV	1402.770	12.65 ± 0.05	7.8 ± 2.1	12.47 ± 0.08	9.9 ± 2.0

^a These results were obtained by the AOD method.

^b The velocity range for component 1 is [-162, -126] km s⁻¹.

^c The velocity range for component 2 is [-126, -90] km s⁻¹.

^d The b -value quoted here is defined as $b_a = [2 \int (v - \bar{v}_a)^2 N_a(v) dv / N_a]^{1/2}$ and integrated over the velocity range for each component.

^e b -values from O VI λ 1031.926 LiF 1A were adopted in finding these upper limits.

the apparent optical depth $\tau_a(v)$. The apparent optical depth is an instrumentally-blurred version of the true optical depth of an absorption feature and is given by

$$\tau_a(v) = -\ln [I(v)/I_c(v)], \quad (1)$$

where $I_c(v)$ is the estimated continuum intensity and $I(v)$ is the observed intensity of the line as a function of velocity. The apparent column density per unit velocity, $N_a(v)$ [atoms cm^{-2} $(\text{km s}^{-1})^{-1}$], is related to the apparent optical depth by

$$N_a(v) = \frac{m_e c \tau_a(v)}{\pi e^2 f \lambda} = 3.768 \times 10^{14} \frac{\tau_a(v)}{f \lambda}, \quad (2)$$

where λ is the wavelength in \AA , and f is the atomic oscillator strength. We adopt rest wavelengths and f -values from Morton (2003). Resolved saturated structure is not seen in any of the profiles, but if present, would be clearly identifiable. Unresolved saturated structure can be identified by comparing the $N_a(v)$ profiles for different transitions of the same species; a smaller apparent column density in the stronger transition suggests saturation. In regions of the profiles for which unresolved saturated structure is not significant, the integrated apparent column density, N_a , is equivalent to the true column density, N . For cases where unresolved saturated structure becomes significant, the apparent column density is a lower limit to the true value. The integrated values of v_a , b_a , and $\log N_a$ are obtained from $v_a = \int v N_a(v) dv / N_a$, $b_a = [2 \int (v - \bar{v}_a)^2 N_a(v) dv / N_a]^{1/2}$, and $N_a = \int N_a(v) dv$, where the integration is performed over the absorption region noted in Table 2.

According to Savage & Sembach (1991), the AOD method is adequate for data with $b_{\text{line}} \sim 0.25\text{--}0.50 b_{\text{inst}}$, where b_{line} is the intrinsic b -value of the line and b_{instr} is the b -value of the instrument. Since $b \equiv \text{FWHM}/1.667$, for STIS E140M, $b_{\text{inst}} \simeq 4 \text{ km s}^{-1}$ and for *FUSE*, $b_{\text{inst}} \approx 12 \text{ km s}^{-1}$. Since there is no tracer of cold gas in the HVCs along this line of sight, such as C II* or C I, it is very unlikely that there is any absorption line with $b \ll 1 \text{ km s}^{-1}$.

When $\tau_a \ll 1$, unresolved saturation should not be problematic as long as b is not much smaller than 1 km s^{-1} . For stronger lines, unresolved saturated structure can be identified by comparing the lines of the same species with different $f\lambda$. Following Savage & Sembach (1991), the difference in $f\lambda$ must be a factor of 2 (or 0.3 dex) or more to be able to detect the effects of unresolved saturation. If some moderate saturation exists, we can correct for it using the procedure described in Savage & Sembach (1991). For various cases of blending and line broadening, they found a tight relation between the difference of the true column density and the apparent column density of the weak line against the difference of the strong line and weak line apparent column densities. The needed correction to the apparent column density of the weak line for a given difference between the strong- and weak-line apparent column densities are summarized in their Table 4.

For the C IV and Si IV doublets, the weak lines of the doublet give systematically larger N_a , suggesting that these lines suffer from small saturation (less than 0.02–0.05 dex), although as we argued above, the continua near these lines is complicated and errors in the continuum placement will have a greater effect on the weak

lines. For O VI, because the intrinsic broadening is large, this line is unlikely to be affected by saturation (see Wakker et al. 2003). Because the peak apparent optical depth for the O I, S III, and Fe II lines are $\lesssim 0.16$, these lines are also unlikely to be saturated. For Si II, 5 transitions are available: the strong lines at 1190, 1193, and 1260 \AA show some saturation effects. The apparent column density of Si II $\lambda 1304$ (weakest line) is 0.06 dex larger than the one of Si II $\lambda 1526$, although within 1σ their apparent column densities overlap. Nonetheless, this is an indication of weak saturation (the continuum placement near these lines is straightforward), and we therefore correct for it in our adopted column density by increasing the column density of Si II $\lambda 1304$ by 0.06 dex (see Table 4 in Savage & Sembach 1991). For Al II, we note that the peak apparent optical depth is smaller than for Si II $\lambda 1304$ (0.5 compared to 0.7) and therefore the saturation correction is likely smaller than the error quoted in Table 2 (these two ions very likely probe the same gas given their similar ionization potentials). Finally, for C II, Si III, N II, only strong transitions are available and are likely all saturated. We therefore only quote lower limits for these ions.

For lines which showed no significant absorption, we adopt 3σ upper limits for the equivalent width. We follow Wakker et al. (1996) and calculate the limit on the equivalent width by

$$\sigma(W)_{m\text{\AA}} = 6.5 \times 10^{-3} \frac{\lambda(\text{\AA})}{S/N} \sqrt{hb}, \quad (3)$$

where λ is the rest wavelength, S/N is the signal to noise ratio, h is the velocity dispersion per pixel for the spectrograph (3.22 km s^{-1} for STIS E140M and 3.74 km s^{-1} for *FUSE*), and b is the estimated b -value in km s^{-1} . From this, the 3σ upper limits on the column density are calculated assuming that the lines fall on the linear part of the curve of growth.

Our adopted total column densities (i.e. that include all the absorption between -162 and -90 km s^{-1}) are summarized in Table 4. Note that for C IV and Si IV, we adopt the results from the profile fitting described in the next section, while the measurement for $N(\text{H I})$ is described in § 4.3.

4.2. Component Fitting of the High Ions

The high ions C IV and Si IV are prominent in both HVC components toward ZNG 1. Since there may be overlap between the absorbing regions, we utilize the method of component fitting that allows us to separate the distinct velocity components. We employ software (described in Fitzpatrick & Spitzer 1997) in which we construct a model for the absorption wherein each profile is composed of multiple Maxwellian “clouds” or components. The best-fit values describing the gas are determined by comparing the model profiles convolved with an instrumental line-spread function (LSF) with the data. The three parameters N_i , b_i , and v_i for each component, i , are input as an initial guesses and subsequently varied to minimize χ^2 . The fitting process enables us to find the best fit of the component structure using the data from one or more transitions of the same ionic species simultaneously.

We applied this component-fitting procedure to the C IV and Si IV doublets. In addition to fitting the

TABLE 4
ADOPTED TOTAL INTERSTELLAR
COLUMN DENSITIES

Species	$\log N^a$	Method
H I	16.50 ± 0.06	FIT, COG
C II	> 14.27	AOD
C II*	< 12.44	3σ
C IV	13.71 ± 0.07	FIT
N I	< 12.82	3σ
N II	> 14.07	AOD
N II**	< 13.41	3σ
N V	< 12.84	3σ
O I	13.38 ± 0.08	AOD
O VI	13.46 ± 0.04	AOD
Al II	12.11 ± 0.07	AOD
Si II	13.55 ± 0.03	AOD
Si III	> 13.30	AOD
Si IV	12.86 ± 0.03	FIT
S II	< 13.39	3σ
S III	13.67 ± 0.10	AOD
Fe II	13.07 ± 0.02	AOD

^a All upper limits are 3σ estimates and the velocity range is -162 to -90 km s^{-1} . See § 4 for more details.

profiles, we used the code to simultaneously determine the best fit continuum about each line (see Fitzpatrick & Spitzer 1997). The continuum for each of the four lines was modeled with a fourth-order Legendre polynomial. The continua determined this way are shown as solid lines in Figure 3. The Si IV and C IV ions were fit separately, i.e., we did not assume a common component structure for both ions a priori. The profile fits are shown as solid lines in Figure 4. Examination of the component models reveals a close agreement between the velocity centroids of C IV and Si IV in the HVC region. We call the component at ~ -142 km s^{-1} *component 1*, and the component at ~ -111 km s^{-1} *component 2*. In the low-velocity region of the C IV profiles, we allowed the software to determine, freely, components at $v_{\text{LSR}} \sim -79$ km s^{-1} and ~ -24 km s^{-1} to account for overlap of this low velocity material with the HVCs. Similarly, for Si IV we included components at $v_{\text{LSR}} \sim -24$ km s^{-1} and ~ -18 km s^{-1} .

The results of the component fitting for C IV and Si IV are given in Table 5. The temperature, T , is determined by assuming only thermal broadening. This gives $T \lesssim A(60.6)b^2$ where A is the atomic weight of the ion, and b , the Doppler parameter in km s^{-1} , is obtained from the fit. The temperatures of the gas are likely to be less than these values due to non-thermal motions. These results are discussed in more detail in § 6 in the context of kinematics and ionization.

Since there is a good agreement in the velocity structure between the C IV and Si IV ions in the HVC region, we looked for the same velocity structure in O VI (note that N V is not detected). Although we were able to fit the HVC region of O VI λ 1031 with one component ($v_{\text{LSR}} = -101.2 \pm 2.8$ km s^{-1} , $b = 35.3 \pm 11.5$ km s^{-1} , $\log N = 13.62 \pm 0.04$ cm^{-2}), we were unable to satisfactorily obtain a two-component fit likely due to both the cruder *FUSE* resolution and an intrinsically different velocity distribution of O VI. We discuss the velocity structure of O VI along with the other ions in § 6.

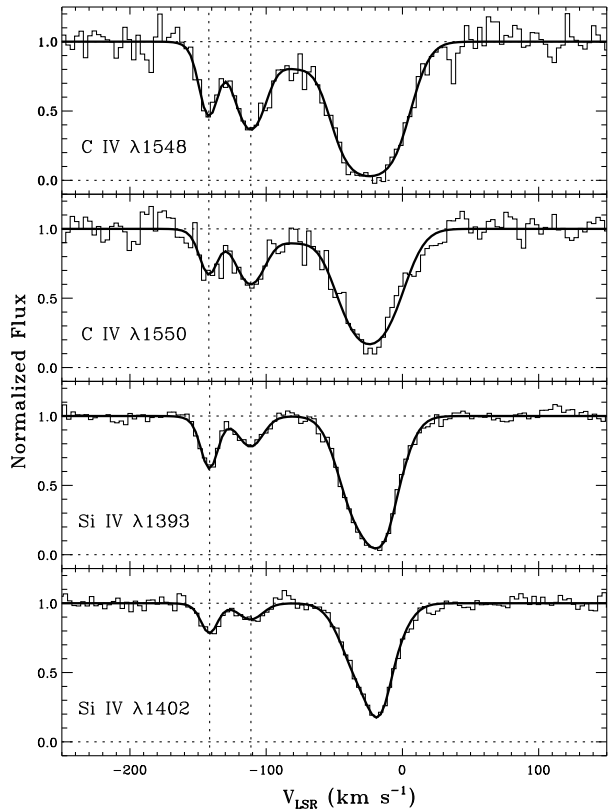


FIG. 4.— The normalized profiles of the ions C IV and Si IV along with the best-fit component model (solid black line). The centroid for component 1 is -142 km s^{-1} and for component 2 is -111 km s^{-1} . The vertical dotted lines represent the centroids derived for each ion.

4.3. H I Column Density Measurements

To estimate the H I column density of the HVC, we used the Lyman series from 926 down to 918 \AA , where the HVC absorption is separated from the stronger H I absorption at higher velocities. In Figure 5, we show the H I profiles of the transitions considered in our measurements from the SiC 2A detector. Higher wavelength transitions were not used because all the components were blended (i.e., the Galactic component is so strong that it covers the weaker absorption at lower velocities). The continuum shown in Figure 5 for each transitions was estimated over a large range of velocities in order to reproduce the overall stellar continuum. The same procedure for the continuum placement was employed for the SiC 1B detector segment.

To estimate the column densities, a curve-of-growth (COG) method and a profile fitting method were used. The COG method used the minimization of the χ^2 error derivation approach summarized by Savage et al. (1990). In Table 6, we summarize the averaged equivalent width measurements estimated in the SiC 2A and SiC 1B profiles. The 1σ errors include continuum and statistical errors. The darkened part of the spectra in Figure 5 shows the typical integration range where the equivalent width was measured. The result from the single-component

TABLE 5
RESULTS OF COMPONENT FITTING OF HIGH ION PROFILES

Species	Component 1 ^a				Component 2 ^b			
	V_{LSR} [km s ⁻¹]	$\log N_a$ [cm ⁻²]	b [km s ⁻¹]	T^c [10 ⁵ K]	V_{LSR} [km s ⁻¹]	$\log N_a$ [cm ⁻²]	b [km s ⁻¹]	T^c [10 ⁵ K]
C IV	-142.1 ± 0.9	13.25 ± 0.06	7.1 ± 1.8	< 0.4 ± 0.2	-111.3 ± 1.4	13.53 ± 0.07	12.8 ± 2.7	< 1.2 ± 0.5
Si IV	-141.5 ± 0.4	12.63 ± 0.03	6.3 ± 0.8	< 0.7 ± 0.2	-111.2 ± 0.9	12.47 ± 0.05	10.6 ± 1.8	< 1.9 ± 0.6

^a The velocity range for component 1 is fixed as [-162, -126] km s⁻¹.

^b The velocity range for component 2 is fixed as [-126, -90] km s⁻¹.

^c T is determined by using $T \lesssim A(60.6)b^2$ where A is the atomic weight and $[b] = \text{km s}^{-1}$. Using both species, we solve for the temperature and the turbulent velocity for each component. We find for component 1: $T \sim 1.4 \times 10^4$ K, $v_{nt} \sim 5.6$ km s⁻¹; for component 2: $T \sim 6.5 \times 10^4$ K, $v_{nt} \sim 8.6$ km s⁻¹.

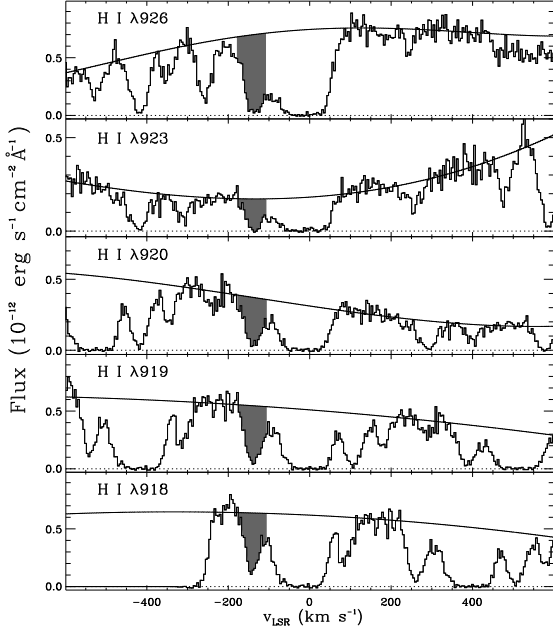


FIG. 5.— *FUSE* SiC2A spectra of the H I transitions used to estimate the HVC H I column density (filled absorption at ~ -140 km s⁻¹). The solid thick lines shows our model for the continuum. The data are binned by 4.2 km s⁻¹ per pixels, the *FUSE* resolution at these wavelengths is ~ 25 km s⁻¹ (FWHM).

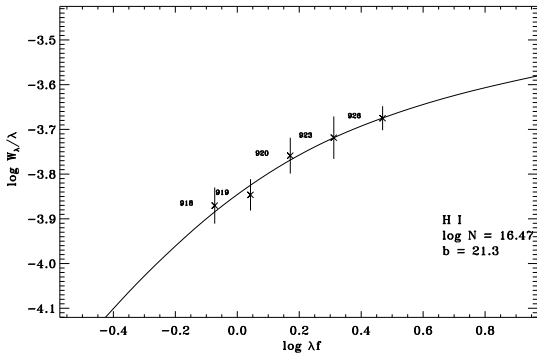


FIG. 6.— Best fit single-component COG for the HVC absorption produced (H I with $b = 21.3^{+2.7}_{-2.4}$ km s⁻¹ and $\log N(\text{H I}) = 16.47^{+0.11}_{-0.08}$). The equivalent widths represent the averages of measurements from the *FUSE* SiC 1B and SiC 2A.

COG is shown in Figure 6, where $b = 21.3^{+2.7}_{-2.4}$ km s⁻¹ and $\log N(\text{H I}) = 16.47^{+0.11}_{-0.08}$.

For the profile fitting, we assume a Gaussian instrumental line spread function with a FWHM = 25 km s⁻¹.

TABLE 6
H I EQUIVALENT WIDTHS FOR THE HVC

λ [Å]	f	W_λ [mÅ]
926.2257	3.18×10^{-3}	195.8 ± 12.5
923.1504	2.22×10^{-3}	176.5 ± 20.4
920.9631	1.61×10^{-3}	160.5 ± 15.5
919.3514	1.20×10^{-3}	131.0 ± 11.0
918.1294	9.21×10^{-4}	123.8 ± 12.1

NOTE. — The equivalent widths represent the average of the SiC2A and SiC1B measurements. We adopt the f -values from Morton (2003).

We simultaneously fit all the H I transitions summarized in Table 6 for both segments, SiC 2A and SiC 1B. In Figure 7, we show an example of this process, where we fitted the absorption with one HVC component and one low velocity component. The result of the fit gives for the HVC component $v = -135.0 \pm 0.8$ km s⁻¹, $b = 21.5 \pm 0.5$ km s⁻¹, and $\log N = 16.48 \pm 0.02$, which is consistent with the COG result although with much smaller errors. However, the absorption in both the local and HVC shows multiple components. Considering the O I $\lambda 1302$ profile (which is the best proxy for the H I profiles), the HVC has at least two components, at -140 km s⁻¹ and -125 km s⁻¹. Considering the S II profile, the local absorption reveals at least two components. Importantly, the singly-ionized species systematically show intermediate-velocity absorption at -59 km s⁻¹, and from our profile fitting trials (see below), its strength and broadening can affect the total column density of the HVC. In the N I absorption profile, this component is not observed. In the O I $\lambda 1302$ profile, the -59 km s⁻¹ component is blended with P II $\lambda 1301$. Unfortunately, P II $\lambda 1152$ has an apparent optical depth near unity; thus the 0.3 dex larger column density measured in P II $\lambda 1301$ relative to P II $\lambda 1152$ is consistent with some saturation in the latter transition or with contamination of the P II $\lambda 1301$ by intermediate velocity absorption from O I $\lambda 1302$. Therefore, it is not clear how much O I absorption there is at -59 km s⁻¹, if any. The O I profiles in the *FUSE* bandpass provide no additional information. There is likely some H I absorption at -59 km s⁻¹, but since the singly-ionized species trace both neutral and ionized gas, it is not clear how strong and broad the H I absorption is in this region.

To test the robustness of the previous fit with 2 com-

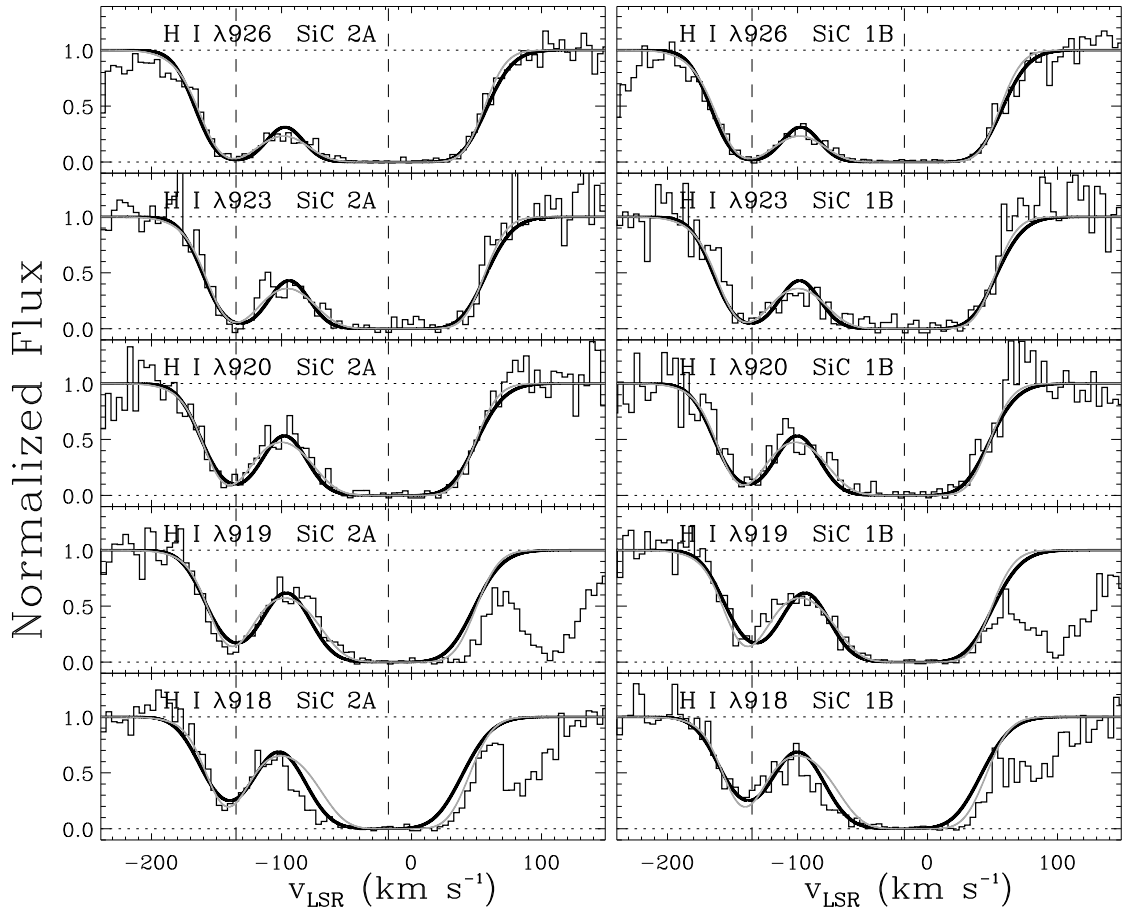


FIG. 7.— Normalized H I profiles against the LSR velocities. The left-hand side shows data from SiC2A, the right-hand side shows data from SiC1B. The black solid line shows the fit to the H I transitions where the velocity centroid of each component is depicted by the dashed line. The grey dotted lines show an example of a fit with 4 components, where the velocities are -140 , -125 , -59 , -7.9 km s^{-1} as suggested by the metal lines. In the two-component fit, the total H I column density for the HVC is 16.48 dex, while in the four-component fit, it is 16.58 dex. Note that the excess absorption in the H I $\lambda\lambda 918, 919$ lines is due to contamination from other absorption lines.

ponents, we modeled the H I lines using several combinations of parameters, including fits with 5 components centered at -140 , -125 , -59 , -6 , $+12$ km s^{-1} and 4 components (removing the $+12$ km s^{-1} component), where all the parameters were allowed to vary (except the velocity at -59 km s^{-1}) or where some parameters were fixed (for example, b and v in the -59 km s^{-1} component). We show in Figure 7 an example of a four-component fit where all the parameters were allowed to vary except for the velocity centroids of the HVC and intermediate-velocity cloud. The result of our robustness trial is that the total H I column density in the HVC ranges from 16.44 to 16.60 dex depending on the assumptions. The reduced- χ^2 is within 10% in all our profile fitting trials. Our fitting results give a mean H I column density of $\log N(\text{H I}) = 16.52 \pm 0.08$. Since the COG and fit methods explore different χ^2 parameters, we adopt a weighted average of the COG and profile fitting results. Our adopted weighted-average (total) H I column density of the HVC is $\log N(\text{H I}) = 16.50 \pm 0.06$.

We note that the single-component fit to the H I provides a firm upper limit to the temperature of component 1: $T \leq (2.80 \pm 0.13) \times 10^4$ K. Because this single component is known to be a combination of multiple absorbing regions, the non-thermal broadening is significant. The

H I-bearing gas making up component 1 is thus quite cool.

5. PHYSICAL CONDITIONS AND CHEMICAL ABUNDANCES IN THE HVC

5.1. Electron Density

We make use of the C II $\lambda 1334$ and C II* $\lambda 1335$ lines to calculate an upper limit to the electron density. The C II* line arises out of the $^2P_{3/2}$ upper fine structure level, which has an energy $E_{12} \sim 8 \times 10^{-5}$ eV above the $^2P_{1/2}$ ground state, out of which the C II transition arises. The excitation in regions of at least moderate ionization (see § 5.3) is dominated by electrons, while the deexcitation should proceed principally via spontaneous radiative decay. Following Spitzer’s (1978) discussion of the excitation balance, the electron density is related to the column density ratio $N(\text{C II}^*)/N(\text{C II})$ by (Lehner et al. 2004):

$$n_e = 0.53 \frac{T^{1/2}}{\Omega_{12}(T)} e^{(E_{12}/kT)} \frac{N(\text{C II}^*)}{N(\text{C II})} \quad (4)$$

where $\Omega_{12}(T)$ is the temperature-dependent collision strength from Blum & Pradhan (1992) and Keenan et al. (1986). This yields an upper limit to the electron density because the column of C II $\lambda 1334$ is a lower limit due to

saturation and C II* $\lambda 1335$ is an upper limit. Using the limit to C II* for the combined HVCs toward ZNG 1 we find $n_e \lesssim (0.36 \text{ cm}^{-3}) T_4^{1/2} (3\sigma)$ for $T_4 \equiv T/(10^4\text{K}) \sim 1$ to 5 within a few percent. The density limit rises to $n_e \lesssim 1.5 \text{ cm}^{-3}$ for $T_4 = 10$, but the collision strengths for $T_4 \gtrsim 5$ are extrapolated from the lower temperature calculations and thus are uncertain. At such temperatures, the ionization fraction of C II should be small, as well.

Si II may be used as a proxy for C II. If one assumes solar relative abundances, the implied column density of C II is $\log N(\text{C II}) \approx 14.43$. Depletion is unlikely to affect this estimate much, as Si II and C II likely have similar depletion characteristics in clouds with “halo cloud” (Sembach & Savage 1996) abundances. Differing ionization levels for C and Si could affect this determination. Adopting $\log N(\text{C II}) = 14.43$, we find $n_e \lesssim (0.25 \text{ cm}^{-3}) T_4^{1/2} (3\sigma)$ for the high velocity gas.

These estimates assume C II* is distributed like C II, where $\gtrsim 2/3$ of the column is associated with component 1. If one individually assesses the densities for components 1 and 2, the limits (3σ) are $n_e \lesssim (0.55 \text{ cm}^{-3}) T_4^{1/2}$ and $\lesssim (0.95 \text{ cm}^{-3}) T_4^{1/2}$ for components 1 and 2, respectively.

5.2. Gas-Phase Abundance

Since O I and H I have nearly identical ionization potentials and are strongly coupled through charge exchange reactions (Field & Steigman 1971), $N(\text{O I})/N(\text{H I})$ can be used as a reliable metallicity indicator. The ionization corrections relating O I/H I to O/H are extremely small.

We have measured a total O I column density of $\log N(\text{O I}) = 13.38 \pm 0.08$ and a total H I column density of $\log N(\text{H I}) = 16.50 \pm 0.06$. Thus the abundance of oxygen is $\log \text{O/H} = -3.12 \pm 0.10$. Assuming the solar abundance of oxygen is $\log \text{O/H} = -3.34 \pm 0.05$ (Asplund et al. 2005), the gas phase abundance of the high velocity gas is then $[\text{O/H}] = +0.22 \pm 0.10$, where $[\text{X/Y}] = \log[N_X/N_Y] - \log\{X/Y\}_\odot$.⁶ Thus, the neutral gas in the HVCs toward ZNG 1 has a super-solar oxygen abundance, the highest measured for any HVC. We assume this abundance is representative of the highly-ionized HVC gas as well.

The measured HVC abundance is high compared with the current best solar abundance, the interstellar gas-phase abundance of oxygen in the solar neighborhood ($\log \langle \text{O/H} \rangle = -3.41 \pm 0.01$, which is likely affected by modest depletion; Cartledge et al. 2004), the average abundance of young F and G dwarfs in the solar neighborhood ($\log \langle \text{O/H} \rangle = -3.35 \pm 0.15$; Sofia & Meyer 2001), and the abundances of H II regions in the solar neighborhood ($\log \langle \text{O/H} \rangle = -3.58$ to -3.33 ; Rudolph et al. 2006 and references therein). While determinations of the solar oxygen abundance have varied significantly recently, the gas-phase oxygen abundance in the HVCs toward ZNG 1 is larger than, or at least consistent, with all of the determinations. These HVCs have significantly higher metallicities than all other known HVCs, and the gas found locally in the Galactic disk. Depletion effects are

unlikely to be significant in this determination; if depletion into the solid phase is important, the total gas+dust phase abundance of the HVCs would be even larger.

5.3. Ionization Fraction

We can estimate the fraction of the gas that is ionized by comparing the H I column with an estimate of the total column density of hydrogen ($N(\text{H}) \equiv N(\text{H I}) + N(\text{H II})$, where we assume H_2 is negligible). We estimate the total H column from the total column of Si: $N(\text{H}) \approx N(\text{Si}) (\text{Si/H})^{-1}$, where $N(\text{Si}) \gtrsim N(\text{Si II}) + N(\text{Si III}) + N(\text{Si IV})$. The inequality arises because Si III is saturated, and we do not have observations of higher stages of ionization (though these should make little contribution). We adopt $\log(\text{Si/H}) = \log(\text{Si/H})_\odot + 0.22 = -4.27$, which assumes solar relative Si/O and a base Si abundance from Asplund et al. (2005). In regions with significant dust, the gas-phase Si/O may be subsolar. We assume the conditions in this gas are such that depletion of Si/O is not significant. The total H column derived in this way using the column densities in Table 4 is $\log N(\text{H}) \gtrsim 18.03$, giving $\log N(\text{H I})/N(\text{H}) \lesssim -1.48$. The total H column is $\gtrsim 30$ times that of the neutral column, and the ionization fraction is then $x(\text{H}^+) \equiv N(\text{H}^+)/N(\text{H}) \gtrsim 0.97$. This large ionization fraction implies $N_{\text{H}} \approx N_{\text{H}^+} \approx N_e$, and justifies our assumption in § 7 that $n_{\text{H}} \approx n_e$.

This represents the value for the HVCs integrated over components 1 and 2. Very similar values are derived if the components are taken individually. Assuming the velocity structure of H I follows that of O I, since their ionization fractions are locked together by a strong charge exchange reaction, we use the O I columns integrated over the velocity ranges of components 1 and 2 to estimate H I in each component assuming a constant $\log(\text{O/H}) = -3.12$ (§ 5.2). This approach yields $\log N(\text{H I})/N(\text{H}) \lesssim -1.44$ and -1.56 for components 1 and 2, respectively, implying ionization fractions $x(\text{H}^+) \gtrsim 0.96$ and $\gtrsim 0.97$.

5.4. Path Length Through the HVCs

The results of the previous subsections can be used to estimate the path length through the HVCs. The path length through a cloud is $\Delta l \approx N(\text{H}) n_{\text{H}}^{-1}$ (this assumes constant n_{H} , though we discuss clumpy media below). Because we do not measure the total hydrogen column, $N(\text{H})$, we use Si or C as a proxy for H (as in § 5.3): $\Delta l_{\text{Si}} \approx N(\text{Si}) (\text{Si/H})^{-1} n_{\text{H}}^{-1}$. Using the electron density limits from § 5.1 for n_{H} , we derive $\Delta l_{\text{Si}} > (1.1 \text{ pc}) T_4^{-1/2} (3\sigma)$ for the integrated HVCs. For temperatures consistent with the temperature limits on component 1 (see Table 5), this implies $\Delta l_{\text{Si}} > 0.6 \text{ pc}$. Similar values can be derived using the columns of C II and C IV ($\Delta l_{\text{C}} > (0.5 \text{ pc}) T_4^{-1/2}$). These estimates apply to both components of the HVC, following the discussion of § 5.1, and do not depend on ionization assumptions.

Taking components 1 and 2 individually, and using the electron density limits derived for each in § 5.1, we find limits (3σ) of $\Delta l_{\text{Si}} > (0.25 \text{ pc}) T_4^{-1/2}$ and $> (0.15 \text{ pc}) T_4^{-1/2}$ for components 1 and 2.

Clumping of the gas into regions of different densities cannot lower this value, as the majority of the gas seen in these ions must be at densities consistent with the

⁶ The older solar system abundances of Grevesse & Noels (1992) give $[\text{O/H}] = +0.01 \pm 0.10$.

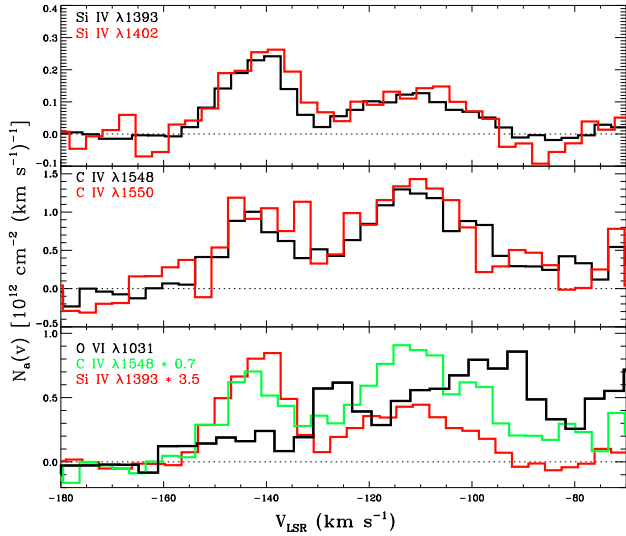


FIG. 8.— A comparison between the apparent column densities of the high ions in the ZNG1 sight line. The top two panels show both lines of the Si IV and C IV doublets. The good agreement between the profiles of each member of the doublet implies little saturation. The bottom panel shows O VI with scaled versions of Si IV and C IV.

limits from C II*. If a large fraction of the column of gas were in high density clumps, C II* absorption would be present. These path lengths are inconsistent with typical sizes of circumstellar matter (e.g., discussion in Sahai et al. 2007). We discuss this further in Section 7.

6. VELOCITY STRUCTURE, KINEMATICS, AND IONIZATION STRUCTURE

6.1. Profile Comparisons

Comparing the apparent column density profiles of the high and low ions provides a visual means by which we can examine the kinematic structure of these species. Figure 8 shows the apparent column density vs. v_{LSR} for the high ions Si IV, C IV, and O VI. Two velocity components are clearly observed in Si IV and C IV with LSR centroid velocities of roughly -140 and -110 km s^{-1} . The centroid velocities of the components coincide well between the two ions (see Table 5) indicating that these ions reside in the same gas.

The C IV/Si IV ratio changes significantly from component 1 to component 2 (Figure 8). Si IV is more prominent in component 1 than component 2 ($\log N_a = 12.63 \pm 0.03$, $\log N_a = 12.47 \pm 0.05$, respectively), but the opposite is true for C IV ($\log N_a = 13.25 \pm 0.06$, $\log N_a = 13.53 \pm 0.07$, respectively). Since C IV has a greater ionization potential than Si IV, this suggests component 2 has a higher degree of ionization, perhaps implying higher temperatures which would be consistent with the results of component fitting (Table 5). This is also supported by the increasing O VI and decreasing low ion contributions. From Figures 9 and 10 we see that more Si III resides in component 2 than does Si IV; yet there is more C IV than Si IV in that component. The ionization potentials for Si III, Si IV, and C IV are 16.3, 33.5, and 47.9 eV, respectively, which suggests that there are at least two processes involved in ionizing that component. The bottom panel of Figure 8 shows the apparent column densities vs. v_{LSR} for the strong lines of C IV, Si IV, and O VI. The velocity distribution of O VI devi-

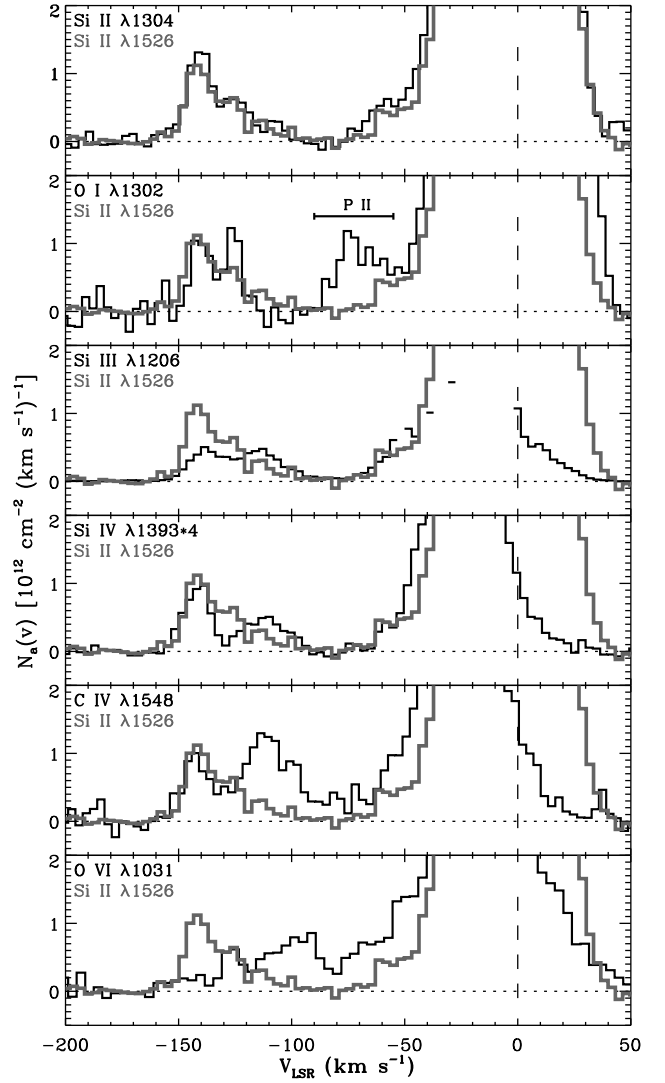


FIG. 9.— Apparent column densities of various ions compared with Si II 1526. The $N_a(v)$ profile for Si IV 1393 is multiplied by a factor of four. Components 1 and 2 have velocity ranges of -162 to -126 km s^{-1} and -126 to -90 km s^{-1} , respectively. The centroid velocities are -142 and -111 km s^{-1} . The ions Si II and O I appear to show a third component with a centroid velocity of ~ -125 km s^{-1} .

ates from the common component structure seen in C IV and Si IV, with an increasing column from $v_{\text{LSR}} \sim -120$ to -90 km s^{-1} . As the columns of C IV and Si IV start to decrease at ~ -110 km s^{-1} , $N(\text{O VI})$ continues to increase up to ~ -90 km s^{-1} , perhaps suggestive of an increase in temperature with velocity leading to higher ionization states.

Figure 9 shows a comparison of the apparent column density profiles of Si II 1526 with the ions Si II 1304, O I 1302, Si III 1206, Si IV 1393, C IV 1550, and O VI 1031. We note that the low ions are mostly confined to $v_{\text{LSR}} \lesssim -125$ km s^{-1} . The low ions reveal a third component with a centroid velocity of roughly -127 km s^{-1} which is not obvious in the profiles of C IV and Si IV. This third component lies roughly between component 1 (-140 km s^{-1}) and component 2 (-110 km s^{-1}). Component 1 appears to be present in the low ions as well as the high ions. However, component 2 is extremely

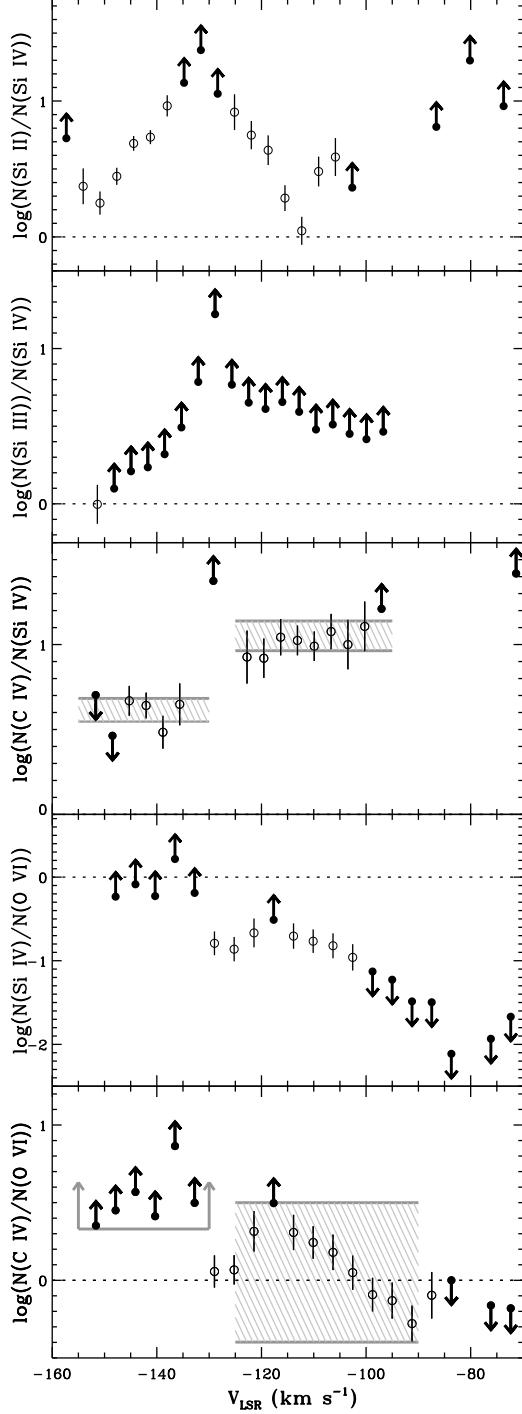


FIG. 10.— Logarithmic apparent column density ratios as a function of v_{LSR} . The ions plotted are Si II $\lambda 1304$, Si III $\lambda 1206$, Si IV $\lambda 1393$, C IV $\lambda 1548$, and O VI $\lambda 1031$. The upward (downward) arrows represent lower (upper) limits. The hatched regions in the C IV/Si IV ratio represent the values derived from component fitting (see Table 7). The hatched region in the C IV/O VI ratio represents the maximum and minimum values for this ratio, although clearly a trend is seen as the ratio decreases toward higher velocities. The light gray arrows in the C IV/O VI ratio represents the lower limit for component 1 (see Table 7). Components 1 and 2 have velocity ranges of -162 to -126 km s^{-1} and -126 to -90 km s^{-1} , respectively.

weak in the low ions. The low ions may show multiple very weak components over the velocity range ~ -135 to -90 km s^{-1} .

6.2. Column Density Ratios and Possible Ionization Mechanisms

Two HVC components are seen in the highly ionized C IV and Si IV, while there are at least 3 components seen in the low ions. The component structure is less certain in the O VI due both to the lower resolution of *FUSE* than STIS and intrinsically broader absorption in O VI. Determining the mechanism(s) by which these species are ionized may aid in constraining the environment in which these HVCs originate.

The principal diagnostics of the ionization mechanisms are the column density ratios of various ions; these can be compared with other sight lines and also with predictions from theoretical models. In Table 7 we report the high ion column density ratios $N(\text{C IV})/N(\text{Si IV})$, $N(\text{C IV})/N(\text{N V})$, and $N(\text{C IV})/N(\text{O VI})$. The ratio $N(\text{C IV})/N(\text{Si IV})$ is derived from the results of component fitting, the ratio $N(\text{C IV})/N(\text{N V})$ is derived from the results of component fitting for C IV and the 3σ upper limit for N V derived from the AOD method, and the ratio $N(\text{C IV})/N(\text{O VI})$ is derived from the ratio of their $N_a(v)$ profiles. Figure 10 shows the ratios of apparent column densities for various ions as a function of v_{LSR} . For the ratios involving O VI (*FUSE*) we smoothed and rebinned the STIS data (Si IV and C IV) to match the resolution and pixel size of *FUSE*.

Component 1 (-162 to -126 km s^{-1}) is characterized by strong absorption in the low ions and weak absorption in O VI. From Figure 10, we place a limit $\log(N(\text{C IV})/N(\text{O VI})) \gtrsim +0.5$ (3σ). If one integrates the O VI over the full velocity range of -162 to -126 km s^{-1} , this ratio is $\log(N(\text{C IV})/N(\text{O VI})) = +0.3 \pm 0.1$. However, the straight integration is dubious since the component structure in C IV appears to be different than that of O VI. The C IV to Si IV ratio seen in Figure 10 is $\log(N(\text{C IV})/N(\text{Si IV})) \sim +0.6 \pm 0.2$, consistent with the results of component fitting. Both Si II and Si III are more abundant than Si IV in this component. We find $\log(N(\text{Si II})/N(\text{Si IV})) \approx +0.7$ for component 1.

The low ions (e.g., O I, Si II) show a component centered between components 1 and 2 of the high ions at $v_{\text{LSR}} \sim -127$ km s^{-1} . There is less or little absorption in O VI, C IV, and Si IV at these velocities. The C IV and Si IV absorption in this region is consistent with the contributions from the wings of components 1 and 2. The O I/Si II ratio in this range is about twice as high as in component 1, suggesting a slightly smaller ionization fraction, $x(H^+) \sim 0.9$.

Component 2 (-126 to -90 km s^{-1}) is characterized by strong O VI absorption and weak absorption for the low ions. From Figure 10, we find $+0.4 \lesssim \log(N(\text{C IV})/N(\text{O VI})) \lesssim +3.2$. Integrating the O VI over the full velocity range of -126 to -80 km s^{-1} gives $\log(N(\text{C IV})/N(\text{O VI})) = +0.1 \pm 0.1$. It is unclear which is more appropriate because the O VI and C IV profiles do not share the same component structure in this velocity range, however, they could be part of the same physical structure. The C IV to Si IV ratio seen in Figure 10 is $\log(N(\text{C IV})/N(\text{Si IV})) \sim +1.0 \pm 0.3$, consistent with the results of component fitting. Both Si II and Si III are

TABLE 7
COMPONENT-TO-COMPONENT COLUMN DENSITY RATIOS^a

Component Number	V_{LSR} [km s ⁻¹]	$N(\text{C IV})/N(\text{Si IV})$	$N(\text{C IV})/N(\text{N V})$	$N(\text{C IV})/N(\text{O VI})$ ^b
1	~ -142	4.2 ± 0.7	> 3.3	> 2.1
2	~ -111	11.5 ± 2.3	> 6.0	$0.4 - 3.2$
Predicted Ratios for Different Ionization Mechanisms ^c				
Radiative Cooling		8.7 – 33.0	0.9 – 2.7	0.0 – 0.2
Radiative Cooling ^d		3.0 – 40.0	0.5 – 13.0	0.1 – 5.0
Conductive Interfaces ^e		5.5 – 30.9	0.8 – 2.6	0.1 – 0.9
Turbulent Mixing Layers ^f		0.9 – 28.8	7.4 – 29.5	1.1 – 7.4
Shock Ionization ^g		1.3 – 33.0	0.7 – 38.6	0.0 – 1.1
Supernova Remnant (SNR) ^h		8.6 – 16.7	2.4 – 2.9	0.1 – 1.9
Halo SNR ⁱ		...	1.8 – 9.0	0.1 – 3.0

^a The values adopted for Si IV and C IV are from Table 5. The values for O VI and N V are taken from Table 3 with N V being 3σ upper limits.

^b The ratios for $N(\text{C IV})/N(\text{O VI})$ are derived from Figure 10 (see text for more details). We quote a lower limit for component 1 and a range for component 2.

^c The references for the collisional ionization mechanisms are: radiative cooling: Heckman et al. (2002), Gnat & Sternberg (2007), Edgar & Chavelier (1986), conductive interfaces: Borkowski et al. (1990), turbulent mixing layers: Slavin et al. (1993), shock ionization: Dopita & Sutherland (1996), SNRs: Slavin & Cox (1992), halo-SNRs: Shelton (1998).

^d The quoted ratios assume gas cooling from 10^6 K with a cooling flow velocity of 100 km s^{-1} for isobaric and isochoric (and intermediate) conditions. The data was taken from Edgar & Chevalier (1986) for the first set of values, and from Gnat & Sternberg (2007) for the second.

^e The quoted ratios assume magnetic field orientations in the range $0 - 85^\circ$, and interface ages in the range $10^5 - 10^7$ yrs. These ratios should be considered crude estimates as they were estimated from graphs in Borkowski et al. (1990).

^f The quoted ratios assume gas with entrainment velocities in the range $25 - 100 \text{ km s}^{-1}$ and mixing-layer temperatures in the range $1 - 3 \times 10^5$ K.

^g The quoted ratios assume shock velocities in the range $150 - 500 \text{ km s}^{-1}$, and magnetic parameters in the range $0 - 4 \mu\text{G cm}^{-3/2}$.

^h The quoted ratios are for SNR ages $10^{5.6-6.7}$ yr.

ⁱ The quoted ratios are for SNR ages $10^{6.0-7.2}$ yr.

also more abundant than Si IV in this component like in the other one, although the Si II to Si IV ratio decreases toward higher velocities.

O VI dominates the region from -100 to -80 km s^{-1} while the Si IV and C IV absorption continues to decline, and there is very little if any absorption in the low ions. This shows that several ionization mechanisms are likely at play.

To investigate the possible mechanisms responsible for the production of the highly-ionized high velocity gas, we focus on Si IV, C IV, N V, and O VI. We compare the ratios of the high ions with those predicted from selected theoretical models in Table 7. Although we compare our results with all these models, we only discuss the models for which all the ratios are consistent with our measured values.

The ratios predicted from the models assume solar relative abundances. Where the models used older estimates of the solar abundance, we have adjusted the results to current solar abundance estimates adopted from Asplund et al. (2005). The adjustments are done following Fox et al. (2004): $\log[N(X)/N(Y)]_{\text{new}}^\odot = \log[N(X)/N(Y)]_{\text{old}}^\odot + \Delta \log A_X^\odot - \Delta \log A_Y^\odot$ where $\Delta \log A_X^\odot \equiv \log A_X^\odot(\text{adopted}) - \log A_X^\odot(\text{old})$. It would however, be preferable to recalculate the models with updated atomic parameters and solar abundances.

In general, the higher stages of ionization become more important as the LSR velocity increases from -150 to -90 km s^{-1} . If collisional ionization dominates the ionization of the high ions, the bottom two panels of Fig-

ure 10 suggest component 2 is at a higher temperature than component 1. If the gas of component 2 were in collisional ionization equilibrium (CIE), it would require temperatures of $(1 - 2) \times 10^5$ K to match the C IV/O VI ratios (Gnat & Sternberg 2007). However, the limits on $N(\text{N V})$ and the strength of Si III are inconsistent with pure CIE.

Of the possible mechanisms that may give rise to the high ions for component 1, only non-equilibrium radiative cooling (RC; Gnat & Sternberg 2007), turbulent mixing layers (TMLs; Slavin et al. 1993, Esquivel et al. 2006), and halo-supernova remnants (halo-SNRs; Shelton 1998) give column density ratios consistent with the observations (see Table 7 and references therein). In the case of radiative cooling, only near the temperature 2×10^4 K do the predicted column densities agree with the observed column densities and ratios. This temperature is allowed by the b -values of this component (see Table 5). However, the RC model predicts a higher Si II to Si IV ratio ($\log N(\text{Si II})/N(\text{Si IV}) \approx 0.8 - 1.0$) than observed in this temperature regime ($\log N(\text{Si II})/N(\text{Si IV}) \approx 0.2 - 0.8$). Therefore, the RC model cannot single-handedly explain the observations. The TML model of Slavin et al. for $\log T = 5.3$ and $v = 100 \text{ km s}^{-1}$, where T is the temperature of the mixing layer and v is the transverse velocity, best matches the observed C IV/Si IV ratio, although our value of 4.17 ± 0.65 is still significantly higher than the metallicity-corrected value this model predicts.⁷ This temperature is also above the maximum tempera-

⁷ The metallicity corrected values are $0.87 - 2.51$, corresponding to velocities of 25 and 100 km s^{-1} , respectively. Our ratio of

ture allowed from component fitting for this component. A velocity higher than the highest they considered (100 km s^{-1}) may improve the agreement given the trends in their predictions. Our C IV/Si IV ratio for component 1 is consistent with the TML models of Esquivel et al. (2006). Esquivel et al. assume ionization equilibrium and their models are evolving, having not reached a steady state.⁸ The Si IV column density was not calculated by Shelton (1998) for her halo-SNR model, so we are unable to test our most stringent ratio against the halo-SNR model for either component.

For component 2, TMLs, shock ionization (SI; Dopita & Sutherland 1996), and halo-SNRs give column density ratios consistent with our measurements. The RC models of Gnat & Sternberg (2007) can match the observed ratios of component 2. However, the total column densities predicted by the models do not match the observed column densities where the ratios are consistent. The observed C IV/Si IV ratio fits best with the TML model of Slavin et al. for $\log T = 5.0$ or 5.5 and $v = 25 \text{ km s}^{-1}$. The highest of these temperatures is inconsistent with the C IV b -value. The TML model of Esquivel et al., on the other hand, seems to be incompatible with our C IV/Si IV ratio. A better agreement may be possible at a lower transverse velocity than the minimum velocity they consider (50 km s^{-1}). The SI model, which matches the observed C IV/Si IV ratio of 11.5 ± 2.3 , has a magnetic parameter of $2\mu\text{G cm}^{3/2}$ and a shock velocity of 200 km s^{-1} . This model could conceivably give similar ratios for the same magnetic parameter but with a velocity somewhere between 300 and 400 km s^{-1} , given the trends in their results.

The multiphase nature of this gas combined with its complicated component structure makes determining the mechanism(s) responsible for the ionization difficult. The ZNG 1 sight line is most likely too complicated to be described by a single model, nor is it likely that the idealized situations in which the models are run encompass the true nature of this gas. We cannot rule out turbulent mixing layers or halo supernova remnants for the -140 km s^{-1} cloud (component 1); similarly, we cannot rule out turbulent mixing layers, shock ionization, or halo supernova remnants for the -110 km s^{-1} cloud (component 2) as possible ionization mechanisms. The kinematics of the HVCs toward ZNG 1 are not inconsistent with these mechanisms.

Given the small b -values for component 1, it may be likely that photoionization also plays an important role in ionizing that component. Although we will show that ZNG 1 itself is unlikely to provide for its ionization, the gas along the ZNG 1 sight line must be subject to radiation escaping from the Milky Way and also the extragalactic background radiation (e.g., see § 6 of Fox et al. 2005). Furthermore, radiation emitted from cooling hot gas could also play a role if these HVCs are in close proximity to such material. Photoionization could explain the presence of C II, Si II, Si III, and the other low ions, and Knauth et al. (2003) showed that it is possible to match our observed C IV/Si IV ratio via photoion-

ization by X-ray/EUV emitting gas. However, neither the Milky Way's escaping radiation nor the extragalactic background radiation can account for the observed O VI (Fox et al. 2005). The ionization of the high ions, and O VI in particular, must involve collisions. Moreover, since the high and low ions seem to coexist in component 1, and possibly throughout parts of component 2, there must be changing physical conditions throughout this multiphase gas.

We finally note that $N(\text{S III}) > 2 \times N(\text{S II})$ in component 1, as well as integrated over the HVCs (see Table 4). This is unusual for gas in the Milky Way. It is in contrast with the ionization state of the photoionized warm ionized medium of the Galaxy for which S II makes up $\sim 75\%$ of the sulfur (as demonstrated by Haffner et al. 1999 and the data given in Howk et al. 2006). This also suggests a relatively high state of ionization for this gas, even for the component that seems likely to be affected by photoionization. This may be reflecting the presence of hot collisionally-ionized material or of a strong, hard ionizing spectrum (but not so hard that it overionizes Si since in component 1 $N(\text{Si IV}) < N(\text{Si III})$). Helium recombination radiation could play a role in ionizing S II to S III.

7. THE CIRCUMSTELLAR HYPOTHESIS

Here we examine the hypothesis that the HVCs seen toward ZNG 1 represents circumstellar material near ZNG 1 itself. As a PAGB star, ZNG 1 may be expected to have some circumstellar material. Although ZNG 1 is sufficiently hot to provide for the ionization of a planetary nebula (PN), no $\text{H}\alpha$ emission is detected about this star (Napiwotzki & Heber 1997). PAGB stars in globular clusters seem less likely to give rise to a visible planetary nebula phase than their field star brethren (Moehler 2001).

The high-velocity gas along this sight line is significantly different than planetary nebula gas. The velocity of the HVCs relative to the stellar photosphere is ~ -150 to -190 km s^{-1} , much higher than planetary nebulae studied in absorption (e.g., K648 in M 15 has an expansion velocity of $12\text{--}17 \text{ km s}^{-1}$ according to Bianchi et al. 2001, while the young PN ESO 457-2 studied by Sterling et al. 2005 shows an expansion of only $\sim 30 \text{ km s}^{-1}$). Furthermore, the columns of material in PNe are typically significantly larger than those seen here (e.g., Williams et al. 2003, Sterling et al. 2005), with many showing very strong absorption from high ions (e.g., C IV) or from excited fine structure states (e.g., S III*, O I*, Si II*; see Sterling et al. 2005, Williams et al. 2003, 2008). The latter are a reflection of the relatively high densities of PN shells, with values $n_e > 1000 \text{ cm}^{-3}$ being the norm (Williams et al. 2003, Sterling et al. 2005, 2007). These densities are in strong contrast to the upper limit of $n_e \leq (0.36 \text{ cm}^{-3})T_4^{1/2}$ reported in Section 5.

While the high velocity gas seen toward ZNG 1 seems unlikely to represent a traditional planetary nebula about the star, it could still be circumstellar in nature. In this scenario, the density of the material would be too low and/or the material too close to the star to produce detectable $\text{H}\alpha$ emission. However, the lower limits to the path lengths derived in Section 5.4 are inconsistent with this. In addition, the lack of C II* is inconsistent with

4.17 ± 0.65 is within the preadjusted range of $1.58\text{--}4.57$ based on the abundances of Grevesse (1984).

⁸ The models of Slavin et al. do not assume ionization equilibrium. They differ from Esquivel et al. in that they predict the column densities assuming a steady state has been reached.

gas very near the star, where radiative pumping can play a role in populating the upper $^2P_{3/2}$ fine structure level of C II. For example, Trapero et al. (1996) observed circumstellar HVC gas (at LSR velocities of -158 and -51 km s $^{-1}$) associated with the close binary η Tau. They observed C II* $\lambda 1335$ absorption which was much stronger than the C II $\lambda 1334$ absorption in the spectra of both stars of the binary, with optical pumping from η Tau responsible for the strong C II*.

Nonetheless, in order to strongly rule out the circumstellar hypothesis we also investigate photoionization models of material about the star ZNG 1. Any circumstellar material is going to be strongly affected by the radiation from the central star. We should be able to produce models consistent with the observations of the HVCs if this is the case. The results of these models strongly suggest this hypothesis is not viable.

We use the Cloudy ionization code (version 07.02.00; last described by Ferland et al. 1998) to calculate the ionization structure of gas about ZNG 1. The ionizing spectrum is assumed to be a model stellar atmosphere calculated with TLUSTY (Hubeny & Lanz 1995). We assumed an effective temperature $T_{\text{eff}} = 45,000$ K and a surface gravity $\log g = 4.48$ with a luminosity $\log L/L_{\odot} = 3.5$ (see Table 1). The elements H, He, C, and N were treated in non-LTE, while other elements were treated in LTE. We assume the atmosphere is made up of 99% He (by number), with C and N at 10 times the solar abundance (by total mass), and O at twice solar. All other elements were scaled to solar abundances except Fe, for which we adopt $[\text{Fe}/\text{H}] = -1.27$. Shocks within the wind of ZNG 1 might produce X-rays, and we have tested the effects of including wind-produced X-rays. For this, we assume emission from a $T = 10^6$ K plasma with a luminosity relative to the stellar bolometric luminosity of $L_X/L_{\text{bol}} = 10^{-7}$ (e.g., Pallavicini et al. 1981). The inclusion of X-rays has very little impact on our models.

We assume the gas is distributed in a constant density shell with $n_{\text{H}} = 0.4$ cm $^{-3}$. This is equivalent to the 3σ limit to the electron density from the integrated C II* diagnostic (the photoionized gas from the models has a temperature $T \approx 10^4$ K) or a 2σ limit for component 1 alone (see § 5.1). The gas is nearly fully ionized, so $n_{\text{H}} \approx n_e$. We adopt a gas-phase metallicity of $\log Z/Z_{\odot} = +0.20$ given our $[\text{O}/\text{H}]$ measurement, and assume solar relative abundances. (The relative solar abundances of the gas should not be compared with those of the photosphere, which has negligible hydrogen. The HVCs, if circumstellar, would represent gas lost from a much different part of the star than as seen as the current photosphere.) We do not include dust for heating or attenuation purposes, but we do include the effects of a Galactic cosmic ray background. We calculate the ionization structure of the gas from an initial inner shell radius, proceeding until the H I column of the HVC is matched. We calculate the total column densities of ions in the gas for inner shell radii in the range $\log(r_0/\text{cm}) = 16.0$ to 20.0, i.e., 0.003 to 33 pc. The lower value is similar to the inner radii of some planetary nebulae (e.g., Sterling et al. 2007). The upper value is unphysically large for such a structure, but we extend the calculations that far to probe the sensitivities of the column densities to this

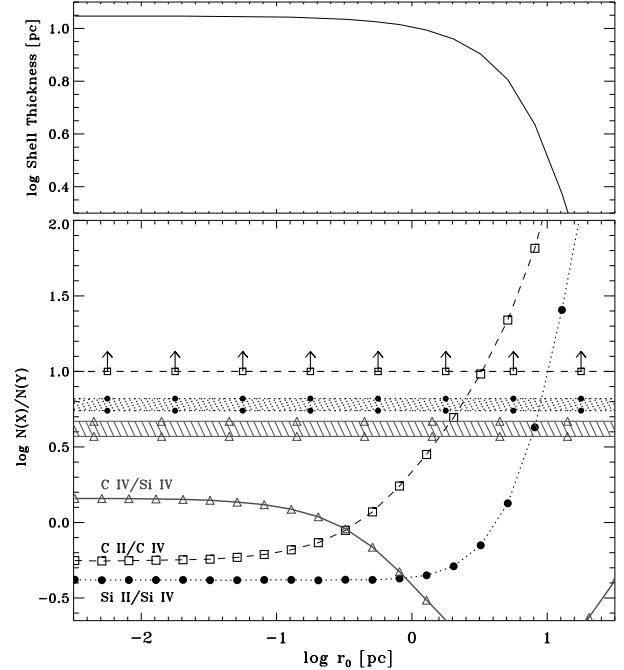


FIG. 11.— Cloudy models of a circumstellar shell about ZNG 1. *Top*: The shell thickness as a function of inner shell radius, r_0 . This depends on the assumed hydrogen density and the ionizing flux of the star. We assume $n_{\text{H}} = 0.4$ cm $^{-3}$, near the upper limit provided by the C II*; lowering the density would increase the shell thickness. *Bottom*: The column density ratios as a function of inner shell radius. We plot the model predictions for the Si II/Si IV, C II/C IV, and C IV/Si IV ratios as the smooth curved lines. The observational constraints for component 1 are shown using the same symbols. The lower limit is for C II/C IV given the likely saturation in the C II profile. The $\pm 1\sigma$ range is shown for the other two ratios. The C IV/Si IV ratio (triangles) cannot be matched by our models. The Si II/Si IV ratio is matched for an inner shell radius of ≈ 9 pc, which is consistent with the constraint provided by C II/C IV. As discussed in the text, the C IV/Si IV ratio for the integrated HVC is even further from the models.

parameter.

The results of the photoionization models are inconsistent with a circumstellar origin for the HVC toward ZNG 1 for a number of reasons. Similar to Section 5.4, the most fundamental difficulty is the predicted thickness of the resulting shell, which is shown in the top panel of Figure 11. Because the limits on the density are so low, a large thickness is required to match the observed H I column density of the HVC. For all models with inner shell radii $r_0 < 1$ pc, the thickness of the shell exceeds 10 pc, implying a shell diameter in excess of the core radius and the half-mass radius of the globular cluster M5 itself (Harris 1996). It is highly unlikely that a shell of such thickness and low density could survive in this environment. Furthermore, such sizes are well in excess of typical PN size scales, as well as typical sizes for circumstellar material observed about typical PAGB stars (see e.g., discussion in Sahai et al. 2007). To find shells with thicknesses < 2 pc requires $r_0 \gtrsim 20$ pc; once again, such a large inner surface to the shell is inconsistent with a circumstellar origin.

We stress that the derived thicknesses are robust predictions of the models dependent only on the adopted density, the H I column density, and the ionizing luminosity of the star. The low density and large luminosity of

the star drive the density of *neutral* hydrogen to very low values, thereby requiring a large path length for even the very low H I column of this HVC. The predicted thickness is insensitive to the presence of X-rays from the wind of ZNG 1. This calculation should also be insensitive to the details of the model stellar atmosphere, so long as the ionizing hydrogen flux is approximately correct (we have tested this sensitivity by calculating models that make use of main sequence OB star atmospheres with similar effective temperatures and surface gravities, finding very similar results). The thickness is, of course, sensitive to the assumed density of the gas. Raising the density to as high as $n_{\text{H}} \approx 1.5 \text{ cm}^{-3}$ seems difficult given the constraints from the C II* absorption and the b -values for component 1 (see Table 4), and that would only decrease the shell thicknesses in Figure 11 by a factor of about four.

We also note that the ionic ratios found in the HVC, either from the total integrated absorption or from the narrow component 1, are difficult to match with our photoionization models. This is shown in the bottom panel of Figure 11. The observed C IV/Si IV ratio cannot be matched by our photoionization models. The maximum C IV/Si IV ratio produced in our models is 1.4, which occurs for $r_0 \lesssim 0.1 \text{ pc}$. This should be compared with the observed ratio of 4.2 ± 0.7 (Table 6) for component 1, which has a lower b -value and displays more prominent low ion absorption than component 2, suggesting it is more likely to be photoionized. The observed C IV/Si IV ratio for the integrated HVCs (components 1 and 2) is 7.1 ± 1.0 . The C II/C IV and Si II/Si IV ratios, which are independent of the assumed relative abundance, can both be matched at large values of the inner radius, r_0 . The limit to the C II/C IV ratio for component 1 is matched for $r_0 \gtrsim 3 \text{ pc}$ ($\gtrsim 1.5 \text{ pc}$ for the integrated ratio), while the Si II/Si IV ratio is matched for $r_0 \approx 9 \text{ pc}$ for both the component 1 and the integrated ratios. The total column densities of C IV and Si IV predicted by the models are not consistent with the data at the same values of r_0 required to match their ratio. Negligible O VI is produced via photoionization.

The difficulty in matching the C IV/Si IV ratio and the large inner shell radii required by the other ionic ratios suggest that the HVC is not ionized directly by ZNG 1. This is, of course, dependent on the shape of the stellar spectrum over the energy range 33 eV to $\gtrsim 65 \text{ eV}$. We have tested the effects of adopting alternative model atmospheres. CoStar model atmospheres (Schaerer & de Koter 1997) of main sequence stars with similar temperatures can match the C IV/Si IV ratio observed in these HVCs. However, they cannot simultaneously match this ratio and the C II/C IV and Si II/Si IV ratios, and they too require large path lengths inconsistent with a circumstellar origin. We also note that Smith et al. (2002) have argued the CoStar models produce spectra that are too hard over the 41 to 54 eV range, which could significantly affect the C IV/Si IV diagnostic. While models invoking shock ionization in addition to photoionization by ZNG 1 could be considered, these will tend to drive down the ionization fraction of H I, requiring even thicker shells. In short, we feel a robust conclusion can be drawn from our models and the physical conditions derived above: the properties of the HVCs toward ZNG 1 are inconsistent with the hypothesis that these clouds have a circum-

stellar origin.

8. DISCUSSION

Along the ZNG 1 sight line, high-velocity absorption is seen in O VI, C IV, and Si IV along with lower ionization and neutral states. As we discussed previously, neither a circumstellar origin (see § 7) nor a local origin (e.g., in Loop I; see § 3) is likely for this absorption. The high-velocity absorption toward ZNG 1 therefore represents an example of interstellar highly-ionized HVCs, sharing ionization and other characteristics (e.g., multiphase structure, column density ratios, b -values) with highly-ionized HVCs observed toward extragalactic objects (e.g., Fox et al. 2006). The presence of the high ions, especially O VI, suggests the presence of hot gas (10^6 K) interacting with cooler gas (10^4 K) in the regions giving rise to this absorption. The theoretical models capable of matching the high-ion column densities and column density ratios in these HVCs include turbulent mixing layers, shocks, and supernova remnants. Furthermore, the multiphase nature of this gas implies that more than one ionization mechanism is responsible for the creation of the ions in the HVCs. While collisional ionization is required to explain the O VI and portions of the other high ions, photoionization is likely to play an important role in the lower ionization species.

The O VI absorption toward ZNG 1 is reminiscent of high-velocity “wings” seen in O VI, C III, and H I toward AGNs (e.g., Sembach et al. 2001; 2003, Savage et al. 2005, Fox et al. 2006). These authors do not identify any negative-velocity wings. One interpretation advanced to explain the highly-ionized wings and other HVCs is that they probe a hot Galactic fountain or Galactic wind. In this scenario, supernovae and stellar winds create large overpressurized bubbles that may eject material and energy from the disk into the halo of the Milky Way. Depending on the speeds of the outflow (often at the sound speed of the hot gas), some material can fall back on the disk (this is a fountain scenario, see Shapiro & Field 1976. Houck & Bregman 1990). If the speeds of the outflow are greater than the escape velocity, a galactic wind will push the material beyond the potential well of the Galaxy. Galactic outflows (and the returning material) often have a complex multiphase mixture of cool and hot gas, as revealed by observations of starburst and dwarf galaxies and by galaxy wind models (e.g., see Veilleux et al. 2005, Heckman et al. 2002, Lehner & Howk 2007). The HVCs along the ZNG 1 sight line are complex multiphase structures, consistent with these observations and models, and the presence of high ions suggests they are closely connected to energetic phenomena in the Galaxy. The blueshifted velocities of the HVCs toward ZNG 1 indicate flows (radial or vertical) with a component directed toward the sun. This may be indicative of a large-scale Galactic circulation, where we are seeing the return of material rather than the ejection.

The origins of highly-ionized HVCs in a galactic fountain-type flow is certainly plausible, but it requires that the HVCs originate in the Galaxy. Thus, their metallicities should be near solar and their distances not too great in such a model. The distances of highly-ionized HVCs toward QSOs and AGNs are unknown, and the metallicity estimates for these HVCs often depend sensitively on the specific ionization model adopted

(see below). However, the distance and metallicity of the highly-ionized HVCs toward ZNG 1 are known. The distance of M5 is well determined and places a strict upper limit for the distance to the HVCs of $d < 7.5$ kpc. The metallicity of the HVC gas is $[O/H] = +0.22 \pm 0.10$. Since our metallicity estimate was derived from a comparison of O I and H I, no ionization correction is needed (see § 5.2). Together, the metallicity and distance constraints rule out an extragalactic origin for these HVCs; instead, it seems probable that these clouds are related to energetic phenomena that drive gas flows in the Milky Way. These are the only highly-ionized HVCs confirmed to be within the Galaxy.

The super-solar metallicity suggests these HVCs originated near the central regions of the Galaxy. Smartt & Rolleston (1997) and Rolleston et al. (2000) showed that the oxygen abundance of early B-type main-sequence stars decreases by -0.07 ± 0.01 dex kpc^{-1} as one moves away from the Galactic center. The expected metallicity of disk gas at a radial distance similar to ZNG 1 is thus $[O/H] \sim +0.35$ if we calculate this from the solar neighborhood toward the Galactic center. The metallicity of these HVCs may be less because they originated closer to the sun than M5. On the other hand, if O is depleted by about 0.1 dex, $[O/H]$ of the HVCs toward ZNG 1 would match the O abundance near the Galactic center.

The close proximity of ZNG 1 to the Galactic center, the complex multiphase structure of the high-velocity gas in this direction, its super-solar metallicity, and its large velocities raise the possibility that these HVCs may not only be linked to a Galactic fountain, but in some way to a wind driven from the vicinity of the Galactic center (e.g., Sofue 2000, Yao & Wang 2007). Bland-Hawthorn & Cohen (2003) and Keeney et al. (2006) each produced a phenomenological model of a Galactic nuclear wind. The former produced their model based on *Midcourse Space Experiment* observations of infrared dust emission from the Galactic center and *ROSAT* X-ray observations, while the model of Keeney et al. was developed to explain highly-ionized HVCs along the Mrk 1383 and PKS 2005–489 sight lines. The model presented by Bland-Hawthorn & Cohen has a bipolar wind with initial velocities of $1700 - 3000$ km s^{-1} , rising from the Galactic center in a $\sim 45^\circ$ conical shape, which becomes cylindrical at a height above the plane of ~ 5 kpc and with a radius of ~ 6 kpc. The model described by Keeney et al. is similar to that of Bland-Hawthorn & Cohen, except that the conical shape turns cylindrical at a z -height of ~ 2 kpc and the cylinder has a radius of ~ 1.5 kpc. ZNG 1 lies within the outer bounds of the outflow cone in the wind model of Bland-Hawthorn & Cohen and just outside that of Keeney et al. While the initial velocities at the base of such a wind are high, Sofue (1984) showed that this wind could slow down considerably. The shock velocities of an evolving wind considered by Bland-Hawthorn & Cohen (2003) and Sofue (2000, 1984) are of the order of one to a few hundred km s^{-1} . If the model of Bland-Hawthorn & Cohen is representative of the Milky Way’s nuclear wind, then the highly-ionized HVCs observed toward ZNG 1 may be gas near the leading edge of the conical section of the wind that is falling back onto the Galaxy. Such infall can occur if thermal instabilities form denser gas with too little buoyancy to be supported against gravity.

If a significant amount of material is participating in outflows or fountain-like processes in the inner Galaxy, other sight lines passing through this region should show signs of these flows. A few extragalactic sight lines that are within about $\pm 25^\circ$ longitude from the Galactic center were observed with *FUSE* or STIS, and all of them (with enough signal) show highly-ionized high-velocity absorption. These include ZNG 1 ($v_{\text{LSR}} < 0$), PG 1553+113 ($v_{\text{LSR}} < 0$) (see below), Mrk 1383 ($v_{\text{LSR}} > 0$) (Keeney et al. 2006, Fox et al. 2006), PKS 2005–489 (2 with $v_{\text{LSR}} < 0$) (Keeney et al. 2006, Fox et al. 2006), ESO 141–G55 ($v_{\text{LSR}} > 0$) (Fox et al. 2006), and PKS 2155–304 ($v_{\text{LSR}} > 0$) (Collins et al. 2004, Fox et al. 2006). Similar to the HVCs toward ZNG 1, all these HVCs are multiphase. Therefore, sight lines that pass through or near the central region show the signature of outflow and infalling material, consistent with large circulation motion with the inner regions of the Milky Way. We note that the sight line toward PG 1553+113 ($l = 21^\circ 9$, $b = +44^\circ 0$) lies only $13:1$ from ZNG 1 and shows a high negative velocity O VI absorption detected at 3.5σ (see § 3). The velocity ($-170 \leq v_{\text{LSR}} \leq -100$ km s^{-1}), column density ($\log N(\text{O VI}) = 13.57^{+0.11}_{-0.13}$), and the shape of the O VI profile (see Figure 6 in Fox et al. 2006) are quite similar to those of the HVCs toward ZNG 1, suggesting that this HVC could be part of a similar flow.

Unfortunately, the metallicity for the HVC toward PG 1553+113 cannot be estimated: the column density of H I cannot be measured due to low signal-to-noise ratios in the *FUSE* SiC channel data. For the other sight lines mentioned above, which probe the inner Galaxy, $N(\text{H I})$ is only estimated for two HVCs in the spectrum of PKS 2155–304 (Collins et al. 2004) and estimated with very large uncertainties for one HVC in the spectrum of PKS 2005–489 (Keeney et al. 2006). For PKS 2155–304, we calculate $[O/H] < +0.37$ and $< +1.62$ for the -140 and -270 km s^{-1} clouds, respectively, based on the column densities of O I and H I estimated by Collins et al. (2004). These values *could* be consistent with a super-solar metallicity. On the other hand, photoionization models by Collins et al. give subsolar values of $-0.47^{+0.15}_{-0.24}$ and $-1.20^{+0.28}_{-0.45}$, inconsistent with the origins of these clouds in a Galactic fountain or outflow. We note that these uncertainties only include errors in the column density measurements, with no contribution from uncertainties in the modeling. These model-derived metallicities are highly dependent on the adopted ionizing spectrum and model assumptions. For example, J.C. Howk et al. (2007, in preparation) show that using a QSO-type and QSO+galaxy type radiation fields can produce metallicities that are different by a factor three in IGM absorbers. Collins et al. adopted a QSO-only radiation field, which provided a better fit to the data than a purely stellar radiation field. However, it is not clear how their metallicity estimates would change if their radiation field included ionizing radiation from the Galaxy as well as QSOs. Furthermore, Si IV and C IV were used to constrain their models, even though it is likely that collisional processes may produce part of the absorption of these high ions (see discussion in Collins et al. 2004). For PKS 2005–489, the metallicity is largely unknown given the order of magnitude uncertainty in $N(\text{H I})$. We therefore believe that without a full understanding of the

ionization in highly-ionized HVCs, metallicity estimates derived purely from photoionization models should be considered tentative at best.

Highly-ionized HVCs along the sight lines HE 0226–4110, PG 0953+414 (Fox et al. 2005) and PG 1116+215 (Ganguly et al. 2005) also have metallicities derived from a comparison of O I to H I. The metallicities of the HVCs toward HE 0226–4110 (+175 km s⁻¹ cloud), and PG 1116+215 (+100 and +184 km s⁻¹ clouds) are [O/H] < -0.07, < +0.05, and -0.66^{+0.39}_{-0.16}, respectively. Those values are all $\gtrsim 2\sigma$ lower than the [O/H] measurement for the HVCs toward ZNG 1. The low metallicities may imply an extragalactic origin for these HVCs. This does not affect the hypothesis that the HVCs toward ZNG 1 trace outflows or circulation/feedback in the inner Galaxy since these sight lines do not pass through the central regions of the Galaxy. It is also not clear that these metallicities are significantly subsolar. Like for the H I HVCs, it is very unlikely that highly-ionized HVCs have a single origin. For instance, based on their kinematics and projection on the sky, several highly-ionized HVCs appear to be associated with known H I HVCs such as Complexes A and C, the Magellanic Stream, and the Outer Arm (e.g., see Fox et al. 2006). The HVCs toward ZNG 1 show, for the first time, that some of the highly-ionized HVCs likely have their origins in the Galaxy. We note that the ionization characteristics and physical conditions of the ZNG 1 HVCs are similar to other highly-ionized HVCs (e.g., $N(\text{C IV})/N(\text{Si IV})$, $N(\text{C IV})/N(\text{O VI})$, b -values, multiphase structure). This may imply that similar ionization mechanisms may be at work in creating the high ions, but it also means that highly-ionized Galactic and extragalactic HVCs cannot be easily separated based on their ionization characteristics alone. We finally note that the properties (i.e., no H I 21 cm emission, $|v_{\text{LSR}}| > 100$ km s⁻¹) of the highly-ionized HVCs toward ZNG 1 fit the category of highly-ionized HVCs considered by Nicastro et al. (2003). These authors proposed a Local Group origin for highly-ionized HVCs because it would better explain their kinematic distribution. The highly-ionized HVCs toward the ZNG 1 sight line show that this argument alone is rather weak. Distances and metallicity estimates are key to distinguish Galactic from extragalactic HVCs, but these are most often estimated indirectly for highly-ionized HVCs, relying on photoionization models. More observations of distant stars may allow direct distance limits for other clouds, as we have done for ZNG 1.

If a Galactic nuclear wind exists and produces significant columns of high ions such as Si IV and C IV (that will be observable with the future Cosmic Origins Spectrograph, COS), it should be visible along other sight lines in the general direction of ZNG 1. Stellar sight lines in this region of the sky may be useful for placing distance constraints on the gas, while AGNs could be used to probe its structure, including its velocity structure. The QSO SDSS J150556.55+034226.3, observed with STIS, lies within 5° of ZNG 1. This QSO has been observed with a low resolution mode of STIS, but is bright enough for future high-resolution UV spectroscopy.

Finally, we note that these HVCs could be related to HVC complex L given their relative proximity on the sky and velocities (see § 3). Since the angular separation is

several times the angular extent of the H I component of complex L, this association is, however, by no means firm. H α emission may be useful in not only studying this connection, but also in tracing feedback flows in the inner Galaxy. Haffner (2005) has mapped intermediate and high negative velocity gas toward complex L (at $l > 0^\circ$). He finds pervasive emission in this region at $-95 \leq v_{\text{LSR}} \leq -50$ km s⁻¹. H α emission in this range is seen within 2° of ZNG 1 with the WHAM survey, though not in the pointing nearest ZNG 1. Haffner also finds extended H α emission from ionized gas associated with complex L ($-150 \leq v_{\text{LSR}} \leq -80$ km s⁻¹). Future mapping of this emission and UV absorption with COS of the central region of the Galaxy may reveal a connection between the HVCs studied here and the material associated with complex L. More importantly, such observations bear on the connection of all this matter to feedback-driven flows in the inner Galaxy.

9. SUMMARY

We have presented *Far Ultraviolet Spectroscopic Explorer* and Space Telescope Imaging Spectrograph observations of the PAGB star ZNG 1 which resides in the globular cluster Messier 5, using these data to study the high-velocity gas along this sight line. The major results of this work are as follows.

1. We have analyzed the high velocity absorption toward ZNG 1 and find the presence of Si IV, C IV, and O VI along with lower ionization species such as C II, Si II, N II, O I, Al II, Fe II, and Si III. These high and low ions are observed in the same velocity range, although they do not share the same component structure. We have catalogued the column densities and b -values using primarily the AOD and component fitting methods.
2. We investigated the possibility that the gas along the ZNG 1 sight line is circumstellar. Limits to the electron density of the gas strongly constrain the path length to be $\gtrsim 0.6$ pc, inconsistent with a circumstellar origin. Furthermore, detailed photoionization calculations also argue against a circumstellar origin based on path length and metal ion ratios.
3. We measured the metallicity of the HVCs to be [O/H] = $+0.22 \pm 0.10$ using the O I and H I absorption. This, combined with the well determined distance to the globular cluster M5 where ZNG 1 resides (7.5 kpc), implies that these clouds have a Galactic origin. This is the first evidence that highly-ionized HVCs may be found near the Galactic disk. The ZNG 1 HVCs have the highest metallicity of any known HVCs.
4. We argue that the ZNG 1 HVCs are not associated with Loop I and reside closer to the Galactic center than this structure. We argue that these HVCs may be associated with a Galactic nuclear wind, or Galactic fountain-like circulation in the inner Galaxy, where the HVCs represent gas falling back to the disk.
5. The exact details of the physical processes responsible for the ionization of these HVCs are yet to

be resolved, and it is likely that a complex interplay between several processes is at work. These HVCs are characterized by changing physical conditions, as component 1 (-110 km s^{-1}) is likely to be significantly affected by photoionization consistent with the small b -values and the stronger presence of lower ionization species, while component 2 (-140 km s^{-1}) must be mostly collisionally ionized as required by the strong presence of O VI and less lower ionization species. The theoretical models consistent with the data for component 1 are turbulent mixing layers and halo-supernova remnants; the models consistent component 2 are turbulent mixing layers, shock interfaces, and halo-supernova remnants. At least qualitatively, the complex phase structure is consistent with energetic circulation associated with a Galactic wind or outflow.

6. It will be difficult to firmly identify a population of extragalactic highly-ionized HVCs (including intergalactic Local Group gas or material condensed from an extended Galactic Corona) without direct estimates or limits of distance and metallicity, since

the kinematics and ionization properties of other highly-ionized HVCs observed toward extragalactic sight lines appear similar to those of the HVCs toward ZNG 1.

This work was partially supported by National Science Foundation grant AST 06-07731 and by the National Aeronautics and Space Administration under Grant No. NNX07AG93G through the Science Mission Directorate. This work is based on observations made with the NASA-CNES-CSA *Far Ultraviolet Spectroscopic Explorer (FUSE)* instrument and the NASA-ESA *Hubble Space Telescope (HST)* instrument. *FUSE* is operated for NASA by the Johns Hopkins University under NASA contract NAS5-32985, and *HST* data is obtained from the Space Telescope Science Institute and is operated by the Association of Universities for Research in Astronomy, Inc. under NASA contract NAS5-26555. This research has made use of the NASA Astrophysics Data System Abstract Service and the SIMBAD database, operated at CDS, Strasbourg, France. In addition, WVD recognizes funding from FUSE grant NNG04GC44G.

REFERENCES

- Almy, R.C., McCammon, D., Digel, S.W., Bronfman, L., & May, J. 2000, *ApJ*, 545, 290
- Anders, E., & Grevesse, N. 1989, *Geochim. Cosmochim. Acta*, 53, 197
- Asplund, M., Grevesse, N., Sauval, A.J. 2005, *ASPC*, 336, 25
- Benjamin, R.A. 2004, in *High Velocity Clouds*, ed. H. van Woerden, B.P. Wakker, U.J. Schwarz, & K.S. de Boer, (Dordrecht: Kluwer), 312
- Berkhuijsen, E.M., Haslam, C.G.T., & Salter, C.J. 1971, *A&A*, 14, 252
- Bianchi, L., Bohlin, R., Catanzaro, G., Ford, H., & Machado, A. 2001, *AJ*, 122, 1538
- Blum, R.D., & Pradhan, A.K. 1992, *ApJS*, 80, 425
- Bohlin, R.C., Smith, A.M., Stecher, T.P., Sweigart, A.V., Cornett, R.H., & Hill, J.K. 1983, *ApJ*, 267, L89
- Bland-Hawthorn, J., & Cohen, M. 2003, *ApJ*, 582, 246
- Blitz, L., Spergel, D.N., Teuben, P.J., Hartmann, D., & Burton, W.B. 1999, *ApJ*, 514, 818
- Borkowski, K.J., Balbus, S.A., & Frstrom, C.C. 1990, *ApJ*, 355, 501
- Brown, T.M., et al. 2002, in *HST STIS Data Handbook*, vol. 4.0, ed. B. Mobasher (Baltimore: STScI)
- Carlberg, R. 1999, in *The Formation of Galactic Bulges*, ed. C.M. Carollo, H.C. Ferguson, & R.F.G. Wyse (New York: Cambridge Univ. Press), 64
- Cartledge, S.I.B., Lauroesch, J.T., & Meyer, D.M. 2004, *ApJ*, 613, 1037
- Collins, J.A., Shull, J.M., & Giroux, M.L. 2004, *ApJ*, 605, 216
- Collins, J.A., Shull, J.M., & Giroux, M.L. 2005, *ApJ*, 623, 196
- Collins, J.A., Shull, J.M., & Giroux, M.L. 2007, *ApJ*, 657, 271
- de Boer, K.S. 1985, *A&A*, 142, 321
- de Heij V., Braun, R., Burton, W.B. 2002, *A&A*, 391, 159
- Dixon, W.V., Brown, T.M., & Landsman, W.B. 2004, *ApJ*, 600, L43
- Dixon, W.V., Brown, T.M., Howk, J.C. & Landsman, W.B. 2006, in *ASP Conf. Ser. 348*, ed. G. Sonneborn, H. Moos & B-G. Andersson, (British Columbia, Canada: ASP), 218
- Dixon, W.V., Sahnou, D.J., Barrett, P.E., Civeit, T., Dupuis, J., Fullerton, A. W., Godard, B., Hsu, J.C., Kaiser, M.E., Kruk, J.W., Lacour, S., Lindler, D.J., Massa, D., Robinson, R.D., Romelfanger, M.L., Sonnentrucker, P. 2007, *PASP*, 119, 527
- Dopita, M.A., & Sutherland, R.S. 1996, *ApJS*, 102, 161
- Edgar, R.J., & Chevalier, R.A. 1986, *ApJ*, 310, 27
- Esquivel, A., Benjamin, R.A., Lazarian, A. Cho, J., & Leitner, S.N. 2006, *ApJ*, 648, 1043
- Ferland, G.J., Korista, K.T., Verner, D.A., Ferguson, J.W., Kingdon, J.B., & Verner, E.M. 1998, *PASP*, 110, 761
- Field, G.B. & Steigman, G. 1971, *ApJ*, 166, 59
- Fitzpatrick, E.L. & Spitzer, L. 1997, *ApJ*, 475, 636
- Fox, A.J., Savage, B.D., Wakker, B.P., Richter, P., Sembach, K.R., & Tripp, T.M. 2004, *ApJ*, 602, 738
- Fox, A.J., Wakker, B.P., Savage, B.D., Tripp, T.M., Sembach, K.R., & Bland-Hawthorn, J. 2005, *ApJ*, 630, 332
- Fox, A.J., Savage, B.D., Wakker, B.P. 2006, *ApJS*, 165, 229
- Freeman, K., & Bland-Hawthorn, J. 2002, *ARA&A*, 40, 487
- Ganguly, R., Sembach, K.R., Tripp, T.M., & Savage, B.D. 2005, *ApJS*, 157, 251
- Gibson, B.K., Giroux, M.L., Penton, S.V., Putman, M.E., Stocke, J.T., Shull, J.M. 2000, *AJ*, 120, 1830
- Gnat, O. & Sternberg, A. 2004, *ApJ*, 608, 229
- Gnat, O. & Sternberg, A. 2007, *ApJS*, 168, 213
- Grevesse, N. 1984, *Phys. Scripta*, T8, 49
- Grevesse, N., Noels, A., & Sauval, A.J. 1992, *Coronal Streamers, Coronal Loops, and Coronal and Solar Wind Composition*, 348, 305
- Haffner, L.M. 2005, in *Extra-Planar Gas*, *ASP Conf. Proc. V. 331*, ed. R. Braun, 25
- Haffner, L.M., Reynolds, R.J., Tufte, S.L. 1999, *ApJ*, 523, 223
- Harris, W.E. 1996, *AJ*, 112, 1487
- Heckman, T.M. 2002, in *ASP Conf. Ser. 254, Extragalactic Gas at Low Redshift*, ed. J. Mulchaey & J. Stocke (San Francisco: ASP), 292
- Heckman, T.M., Norman, C.A., Strickland, D.K., & Sembach, K.R. 2002, *ApJ*, 577, 691
- Houck, J.C., & Bregman, J.N. 1990, *ApJ*, 352, 506
- Howk, J.C., Sembach, K.R., & Savage, B.D. 2006, *ApJ*, 637, 333
- Hubeny, I., & Lanz, T. 1995, *ApJ*, 439, 875
- Ibata, R.A., Gilmore, G., & Irwin, M.J. 1994, *Nature*, 370, 194
- Irwin, J.A., Seaquist, E.R., Taylor, A.R., & Duric, N. 1987, *ApJ*, 313, L91
- Kalberla, P.M.W., Burton, W.B., Hartmann, Dap, Arnal, E.M., Bajaja, E., Morras, R., & Pöppel, W.G.L. (2005), *A&A*, 440, 775
- Keenan, F.P., Lennon, D.J., Johnson, C.T., & Kingston, A.E. 1986, *MNRAS*, 220, 571
- Keeney, B.A., Danforth, C.W., Stocke, J.T., Penton, S.V., & Shull, M.J. 2006, *ApJ*, 646, 951
- Kerr, F.J., & Lynden-Bell, D. 1986, *MNRAS*, 221, 1023
- Kimble, R.A., et al. 1998, *ApJ*, 492, L83
- Knauth, D.C., Howk, J.C., Sembach, K.R., Lauroesch, J.T., & Meyer, D.M. 2003, *ApJ*, 592, 964
- Lehner, N., Keenan, F.P., & Sembach, K.R. 2001, *MNRAS*, 323, 904
- Lehner, N. 2002, *ApJ*, 578, 126

- Lehner, N., Wakker, B.P., & Savage, B.D. 2004, *ApJ*, 615, 767
- Lehner, N., & Howk, J.C. 2007, *MNRAS*, 377, 687
- Martin, C.L. 1999, *ApJ*, 513, 156
- Mihalas, D., & Binney, J. 1981, *Galactic Astronomy*, 2nd ed.; (Freeman, San Francisco)
- Moehler, S. 2001, *PASP*, 113, 1162
- Moos, H.W., et al. 2000, *ApJ*, 538, L1
- Morton, D. 2003, *ApJS*, 149, 205
- Münch, G. 1952, *PASP*, 64, 312
- Münch, G., & Zirin, H. 1961, *ApJ*, 133, 11
- Napiwotzki, R. & Heber, U. 1997, in *The Third Conference on Faint Blue Stars*, ed. A.G.D. Philip, J. Liebert, R. Saffer, & D.S. Hayes (Schenectady: L. Davis Press), 441
- Nicastro, F., Zezas, A., Elvis, M., Mathur, S., Fiore, F., Cecchi-Pestellini, C., Burke, D., Drake, J., Casella, P. 2003, *Nature*, 421, 719
- Nicastro, F. 2005, in *IAU Symp. 216, Maps of the Cosmos*, ed. M. Colless, L. Staveley-Smith, & R. Stathakis (San Francisco: ASP), 297
- Norman, C.A., Ikeuchi, S. 1989, *ApJ*, 345, 372
- Oort, J.H. 1970, *A&A*, 7, 381
- Pallavicini, R., Golub, L., Rosner, R., Vaiana, G. S., Ayres, T., & Linsky, J. L. 1981, *ApJ*, 248, 279
- Park, J.-W., Min, K.-W., Seon, K.-I., Kim, I.-J., Lim, Y.-M., Han, W. Nam, U.-W., Park, J.-H., Edelstein, J. Korpela, E.J., & Sankrit, R. 2007, *ApJ*, 665, L39
- Piotto, G. et al. 2002, *A&A*, 391, 945
- Putman, M.E., Staveley-Smith, L., Freeman, K.C., Gibson, B.K., Barnes, D.G. 2003, *ApJ*, 586, 170
- Putman, M. E., Thom, C., Gibson, B. K., Staveley-Smith, L. 2004, *ApJ*, 603, 77
- Richter, P., Westmeier, T., & Brüns, C. 2005, *A&A*, 442, 49
- Richter, P. 2006, preprint (astro-ph/0602343)
- Rolleston, W.R.J., Smartt, S.J., Dufton, P.L., & Ryans, R.S.I. 2000, *A&A*, 363, 537
- Rudolph, A.L., Fich, M., Bell, G.R., Norsen, T., Simpson, J.P., Haas, M.R., & Erickson, E.F. 2006, *ApJS*, 162, 346
- Sahai, R., Morris, M., Sánchez Contreras, C. & Claussen, M. 2007, arXiv:0707.4662, in press
- Sahnow, D.J., et al. 2000, *ApJ*, 538, L7
- Savage, B.D., & Lehner, N. 2006, *ApJS*, 162, 134
- Savage, B.D., Massa, D., & Sembach, K.R. 1990, *ApJ*, 355, 114
- Savage, B.D. & Sembach, K.R. 1991, *ApJ*, 379, 245
- Savage, B.D., Wakker, B.P., Fox, A.J., & Sembach, K.R. 2005, *ApJ*, 619, 863
- Schaerer, D., & de Koter, A. 1997, *A&A*, 322, 598
- Sembach, K.R., Wakker, B.P., Savage, B.D., Richter, P., Meade, M., Shull, J.M., Jenkins, E.B., Sonneborn, G., & Moos, H.W. 2003, *ApJS*, 146, 165
- Sembach, K.R., Howk, J.C., Savage, B.D., Shull, J.M., & Oegerle, W.R. 2001, *ApJ*, 561, 573
- Sembach, K.R., Savage, B.D. 1992, *ApJS*, 372, 81
- Sembach, K.R., Savage, B.D., & Tripp, T.M. 1997, *ApJ*, 480, 216
- Sembach, K.R., Savage, B.D., Lu, L., Murphy, E.M. 1999, *ApJ*, 515, 108
- Shapiro, P.R., & Field, G.B. 1976, *ApJ*, 205, 762
- Shelton, R.L. 1998, *ApJ*, 504, 785a
- Silva, A.I., & Viegas, S.M. 2001, *CPC*, 136, 319
- Silva, A.I., & Viegas, S.M. 2002, *MNRAS*, 329, 135
- Slavin, J.D., & Cox, D.P. 1992, *ApJ*, 392, 131
- Slavin, J.D., Shull, J.M., & Begelman, M.C. 1993, *ApJ*, 407, 83
- Smartt, S.J., & Rolleston, W.R.J. 1997, *ApJ*, 481, 47
- Smith, L.J., Norris, R.P.F., & Crowther, P.A. 2002, *MNRAS*, 337, 1309
- Sofia, U.J., & Meyer, D.M. 2001, *ApJ*, 554, L221
- Sofue, Y. 1984, *PASJ*, 36, 539
- Sofue, Y. 2000, *ApJ*, 540, 224
- Spitzer, L. 1978, *Physical Processes in the Interstellar Medium* (New York: Wiley)
- Spitzer, L., & Fitzpatrick, E.L. 1993, *ApJ*, 409, 299
- Sterling, N.C., Dinerstein, H.L., Bowers, C.W., & Redfield, S. 2005, *ApJ*, 625, 368
- Sterling, N.C., Dinerstein, H.L., & Kallman, T.R. 2007, *ApJS*, 169, 37
- Strickland, D.K. 2002, in *ASP Conf. Ser. 253, Chemical Enrichment of the Intracluster and Intergalactic Medium*, ed. R. Fusco-Femiano & F. Matteucci (San Francisco: ASP), 387
- Thom, C., Putman, M.E., Gibson, B.K., Christlieb, N., Flynn, C., Beers, T.C., Wilhelm, R., & Lee, Y.S. 2006, *ApJ*, 638, 97
- Thom, C., Peek, J.E.G., Putman, M.E., Heiles, C., Peek, K.M.G., & Wilhelm, R. 2007, preprint (astro-ph/0712.0612)
- Trapero, J., Welty, D.E., Hobbs, L.M., Lauroesch, J.T., Morton, D.C., Spitzer, L., & York, D.G. 1996, *ApJ*, 468, 290
- Tripp, T.M., Jenkins, E.B., Bowen, D.V., Prochaska, J.X., Aracil, B., & Ganguly, R. 2005, *ApJ*, 619, 714
- Tufte, S.L., Wilson, J.D., Madsen, G.J., Haffner, L.M., Reynolds, R.J. 2002, *ApJ*, 572, 153
- van Woerden, H., Schwarz, U.J., Peletier, R.F., Wakker, B.P., Kalberla, P.M.W., 1999, *Nature*, 400, 138
- van Woerden, H., & Wakker, B.P. 2004, *High Velocity Clouds*, *ASSL*, 312, 195
- Veilleux, S. 2002, in *ASP Conf. Ser. 254, Extragalactic Gas at Low Redshift*, ed. J. Mulchaey & J. Stocke (San Francisco: ASP), 313
- Veilleux, S., Cecil, G., & Bland-Hawthorn, J. 2005, *ARA&A*, 43, 769
- Wakker, B.P. 1991, *A&AS*, 90, 495
- Wakker, B.P., et al. 1996, *ApJ*, 473, 834
- Wakker, B.P., & van Woerden, H. 1991, *A&A*, 250, 509
- Wakker, B.P., & van Woerden, H. 1997, *ARA&A*, 35, 217
- Wakker, B.P., van Woerden, H., & Gibson, B.K. 1999, in *ASP Conf. Ser. 166, Stromlo Workshop on High Velocity Clouds*, ed. B.K. Gibson & M.E. Putman (San Francisco: ASP), 311
- Wakker, B.P. 2001, *ApJS*, 136, 463
- Wakker, B.P. 2004, *Ap&SS*, 289, 381
- Wakker, B.P., York, D.G., Wilhelm, R., Barentine, J.C., Richter, P., Beers, T.C., Ivezić, Ž., Howk, C. 2007a, preprint (astro-ph/0709.1926), paper I
- Wakker, B.P., York, D.G., Howk, C., Barentine, J.C., Wilhelm, R., Peletier, R.F., van Woerden, H., Beers, T.C., Ivezić, Ž., Richter, P., Schwarz, U.J. 2007b, (in preparation), paper II
- Williams, R., Jenkins, E.B., Baldwin, J.A., & Sharpee, B. 2003, *PASP*, 115, 178
- Williams, R., Jenkins, E.B., Baldwin, J.A., Zhang, Y., Sharpee, B., Pellegrini, E., & Phillips, M. 2008, *ApJ*, in press (arXiv:0801.2147)
- Wolleben, M. 2007, *ApJ*, 664, 349
- Woodgate, B.E., et al. 1998, *PASP*, 110, 1183
- Yao, Y. & Wang, D.Q. 2007, *ApJ*, 666, 242
- Zsargó, J., Sembach, K.R., Howk, J.C., & Savage, B.D. 2003, *ApJ*, 586, 1019